Compression injury regulates astrocyte morphology, metabolic function, and extracellular matrix modification in a 3D hydrogel

Ana N. Strat[a,b,c], Suhani Patel[a], Minh-Tri Ho Thanh[c,d], Alexander Kirschner[a], Souvik Ghosh[a,c], Michael P. Geiss[c,d], Arunkumar Venkatesan[a], Audrey M. Bernstein[a,c,e,f,h], Mariano Viapiano[b], Yutao Liu[f], Alison E. Patteson[c,d], Samuel Herberg[a,c,e,g,h,i], Preethi S. Ganapathy[a,b,c]

Affiliations:

[a]Department of Ophthalmology & Visual Sciences, SUNY Upstate Medical University, Syracuse, NY 13210, USA

[b]Department of Neuroscience and Physiology, SUNY Upstate Medical University, Syracuse, NY 13210, USA

[c]BioInspired Institute, Syracuse University, Syracuse, NY 13244, USA

[d]Department of Physics, Syracuse University, Syracuse, NY 13244, USA

[e]New York VA Health Care, Syracuse VA Medical Center, Syracuse, NY, USA

[f]Department of Cellular Biology and Anatomy, Augusta University, Augusta, GA 30912 , USA

[g]Department of Cell and Developmental Biology, SUNY Upstate Medical University, Syracuse, NY 13210, USA

[h]Department of Biochemistry and Molecular Biology, SUNY Upstate Medical University, Syracuse, NY 13210, USA

[i]Department of Biomedical and Chemical Engineering, Syracuse University, Syracuse, NY 13244, USA

*To whom correspondence should be addressed: Preethi S. Ganapathy MD, PhD; Assistant Professor; Department of Ophthalmology & Visual Sciences, SUNY Upstate Medical University, 505 Irving Avenue, Neuroscience Research Building Room 4606, Syracuse, NY 13210, USA, email: ganapatp@upstate.edu

Keywords: optic nerve head, biomechanical strain, glaucoma, mechanobiology, ECM hydrogels, transcriptomics, morphology

Abbreviations

ATP adenosine triphosphate
ATR ataxia telangiectasia and Rad3 related
CNS central nervous system
ECM extracellular matrix
EGF epidermal growth factor
ETC electron transport chain
F-actin filamentous actin
FBS fetal bovine serum
GFAP glial fibrillary acidic protein
HIF-1α hypoxia-inducible factor 1 α
IL6 interleukin 6
IL17 interleukin 17
IOP intraocular pressure
MONHA mouse optic nerve head astrocyte
ONH optic nerve head
PI3K-Akt phosphoinositide 3-kinase Ak strain transforming
TGFβ2 transforming growth factor beta 2

94 **Graphical abstract**

95

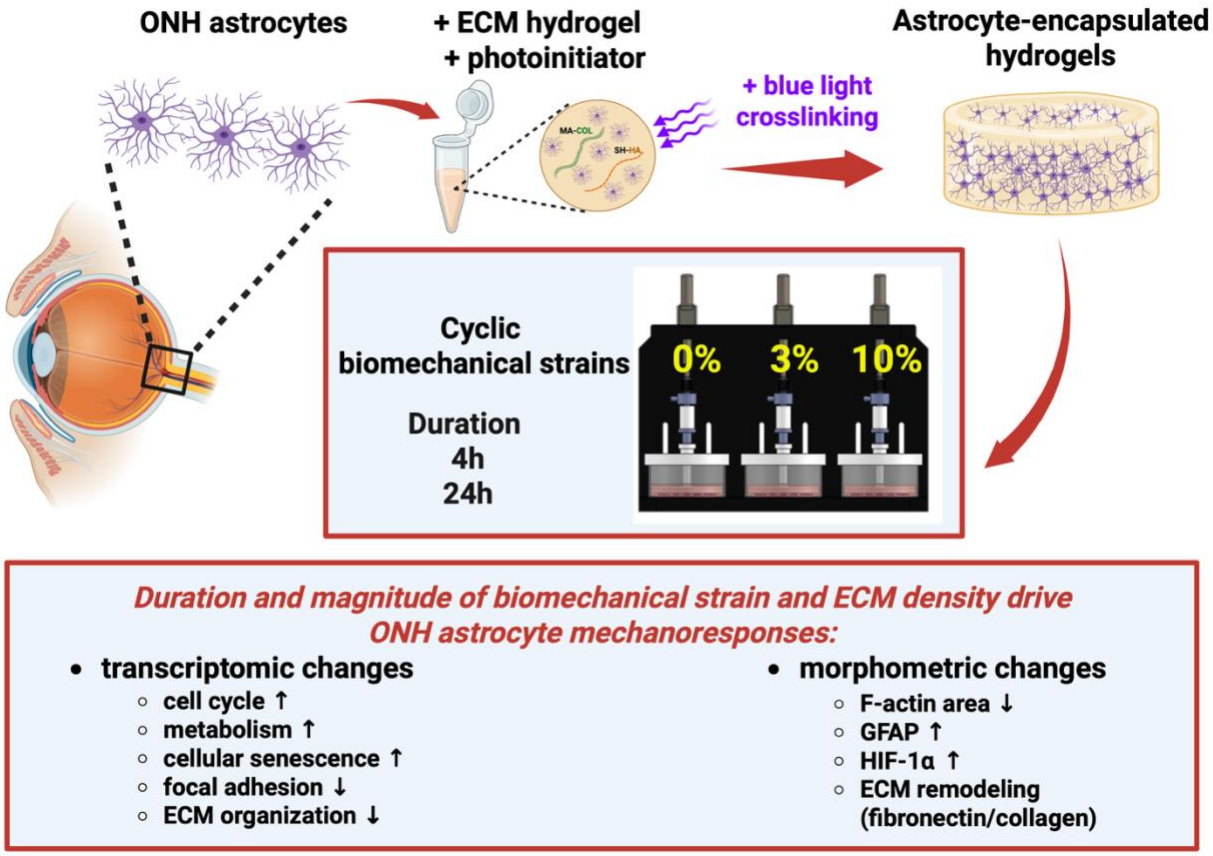

96

97

98

99

100

101

102

103

104

105

Abstract

In glaucoma, the optic nerve head (ONH) is exposed to increased biomechanical strain, impacting the resident astrocytes that maintain neural homeostasis. During disease progression astrocytes exhibit morphologic and metabolic shifts; however, the specific impact of glaucoma-related biomechanical strains on astrocyte behavior remains poorly understood. To address this, we used our previously established 3D cell-encapsulated extracellular matrix (ECM) hydrogel to investigate ONH astrocyte cellular and transcriptomic responses to varying biomechanical strain levels over time. Murine ONH astrocyte were encapsulated within an ECM hydrogel made from photocrosslinkable collagen type I and hyaluronic acid, and subjected to 0, 3, or 10% cyclic compression for 4h and 24h. We found significant restructuring of cytoskeletal morphology, metabolic dysregulation, and astrocyte-mediated ECM modulation that were strain-, duration- and hydrogel subregion-dependent. These phenotypic alterations were associated with diverse transcriptional changes in genes related to cell cycle and morphology, inflammation, metabolism and matrix remodeling that were driven by compressive strain intensity and duration. Our work reveals the direct role of compressive strain in eliciting a complex astrocyte response, supports targeting mechanosensation to prevent these pathologic astrocyte responses, and establishes ECM-based hydrogels as a platform to test mechanisms driving astrocyte mechanodysfunction. Altogether, our study offers new insights into astrocyte responses to biomechanical insult and demonstrates the use of a tunable 3D ECM hydrogel for future mechanistic studies of neurodegeneration.

128 ***1. Introduction***

129 Astrocytes are the master glial cells regulating central nervous system homeostasis. They
130 provide trophic and matrix support to neurons, contribute to modulating synaptic activity and
131 interact with neighboring glial cells and blood vessels to ensure optimal function and protection
132 of neuronal tissue [1-3]. Astrocytes are highly sensitive to biomechanical stimuli, with their
133 development and heterogeneity influenced by the surrounding biomechanical environment [4, 5].
134 Equally important to healthy physiologic conditions is the response of astrocytes to different
135 biomechanical insults within a diseased central nervous system. In neuropathies induced acutely
136 by trauma (e.g., traumatic brain or spinal cord injuries) or chronically by neurodegeneration (e.g.,
137 glaucoma), astrocytes are subjected to pathological biomechanical stimuli of various types,
138 magnitudes, and durations that govern the cellular mechanoresponse [6, 7].

139 In glaucoma, pathologic biomechanical strains are directed upon the optic nerve head
140 (ONH), where there is progressive loss of retinal ganglion cells ultimately leading to irreversible
141 blindness [8, 9]. The local astrocytes within this region provide key support to axons and are first
142 responders to acute glaucomatous insult prior to neuronal dysfunction [10, 11]. Their early
143 response is characterized by a morphologic shift, associated with cytoskeletal protein alterations
144 [10, 12-14]. As the disease progresses, astrocytes decouple from neighboring cells and remodel
145 the surrounding extracellular matrix (ECM) by significantly increasing production of ECM
146 proteins (e.g., fibronectin and collagen IV), matrix crosslinking/degrading enzymes (e.g.,
147 transglutaminase 2 and matrix metalloproteinases 2/9), and pro-fibrotic cytokines (e.g.,
148 transforming growth factor beta 2 (TGFβ2)) [15, 16]. These glial cells are also responsible for
149 matching the metabolic demand of neurons under stress. This metabolic interdependence,

150 exemplified by the glutamate–glutamine cycle and astrocyte-mediated vasodilation, is crucial for
151 neuronal health and its disruption contributes to neurodegenerative diseases [3, 17].

152 Evidence supports that the ONH in glaucoma is subjected to various degrees of
153 compressive and tensile strains that vary by microregion. Specifically, finite element modeling
154 studies predict between 3-10% compressive and 2-5% tensile biomechanical strain on the ONH
155 with intraocular pressure (IOP) elevation [18-20]. While many studies have used such modeling
156 approaches to understand the biomechanical strains within the glaucomatous ONH, there are
157 limited reports on the direct phenotypic and transcriptional responses of local astrocytes to isolated
158 biomechanical strains. This is a crucial gap in our understanding of how glaucomatous
159 biomechanical strains can impact astrocyte behavior and, ultimately, disrupt their functional
160 support of neurons. Prior studies have reported on ONH astrocyte cell cultures subjected to
161 mechanical stressors such as hydrostatic pressure and tension in 2D [17, 21]. While not without
162 merit, conventional 2D *in vitro* culture systems are not suitable to analyze 3D astrocyte
163 morphological complexity and coupling under biomechanical forces. Furthermore, it is nearly
164 impossible to subject monolayer astrocyte cultures to compression in 2D.

165 We previously developed a cell–encapsulated hydrogel containing murine ONH astrocytes
166 and ECM biopolymers (collagen type I and hyaluronic acid), which permits detailed analysis of
167 cell shape and cell–cell/cell–ECM interactions in 3D [22]. In the present study, we investigated
168 how ONH astrocytes that are encapsulated within this ECM hydrogel respond to varying degrees
169 of compressive biomechanical strain over time using a well-established bioreactor [23-25]. We
170 aimed to thoroughly characterize the phenotypic and transcriptional responses of astrocytes to
171 strain magnitude and duration. To achieve this, we conducted histologic analyses and bulk RNA
172 sequencing to determine changes in cytoskeletal organization, metabolic function, ECM

173 remodeling, and gene expression over time. Ultimately, our study represents a comprehensive
174 investigation of time–dependent ONH astrocyte mechanoresponses to glaucoma–relevant
175 biomechanical strains and seeks to provide mechanistic insights into broader astrocyte
176 mechanodysfunction in neurodegenerative diseases of the central nervous system.
177
178 ***2. Results***
179 ***2.1 Characterization of astrocyte-encapsulated hydrogel pore size, permeability, and regional***
180 ***differences***
181 Under healthy conditions, local astrocytes create a honeycomb network spanning the
182 diameter of the rodent ONH [26]. Their processes can measure a thickness of 1.3 ± 0.04 μm with
183 elongations of up to 30 μm [27]. To determine whether our previously developed ECM hydrogel
184 was adequately porous to allow for mouse ONH astrocyte (MONHA) process elongation and
185 coupling through the collagen network, we first quantified the pore size of acellular ECM
186 hydrogels in the absence of biomechanical strain. Using confocal reflectance microscopy to
187 directly visualize collagen fibers within acellular hydrogels, we observed that the collagen fibrils
188 displayed a homogeneous network with pore sizes ranging from 2 – 7 μm (Suppl. Fig. 1A-B).
189 Next, we quantified ECM hydrogel permeability over time (Suppl. Fig. 1C). Since our
190 astrocyte growth media contains primarily fetal bovine serum (FBS) proteins ranging < 60 – 70
191 kDa (with albumin being the most abundant) [28], and added epidermal growth factor which is ~
192 6 kDa [29], we chose to use a 70 kDa FITC-labelled dextran tracer solution as an indicator for
193 permeability. Both the acellular and MONHA-encapsulated hydrogels showed robust
194 permeability, as seen by the rapid detection of increased fluorescence below the ECM hydrogel
195 within 5 minutes of adding FITC-labelled dextran solution to the top of the hydrogels (Suppl. Fig.

196 1C). Thus, these results support that MONHA-encapsulated hydrogels allow for efficient and

197 adequate nutrient distribution.

198

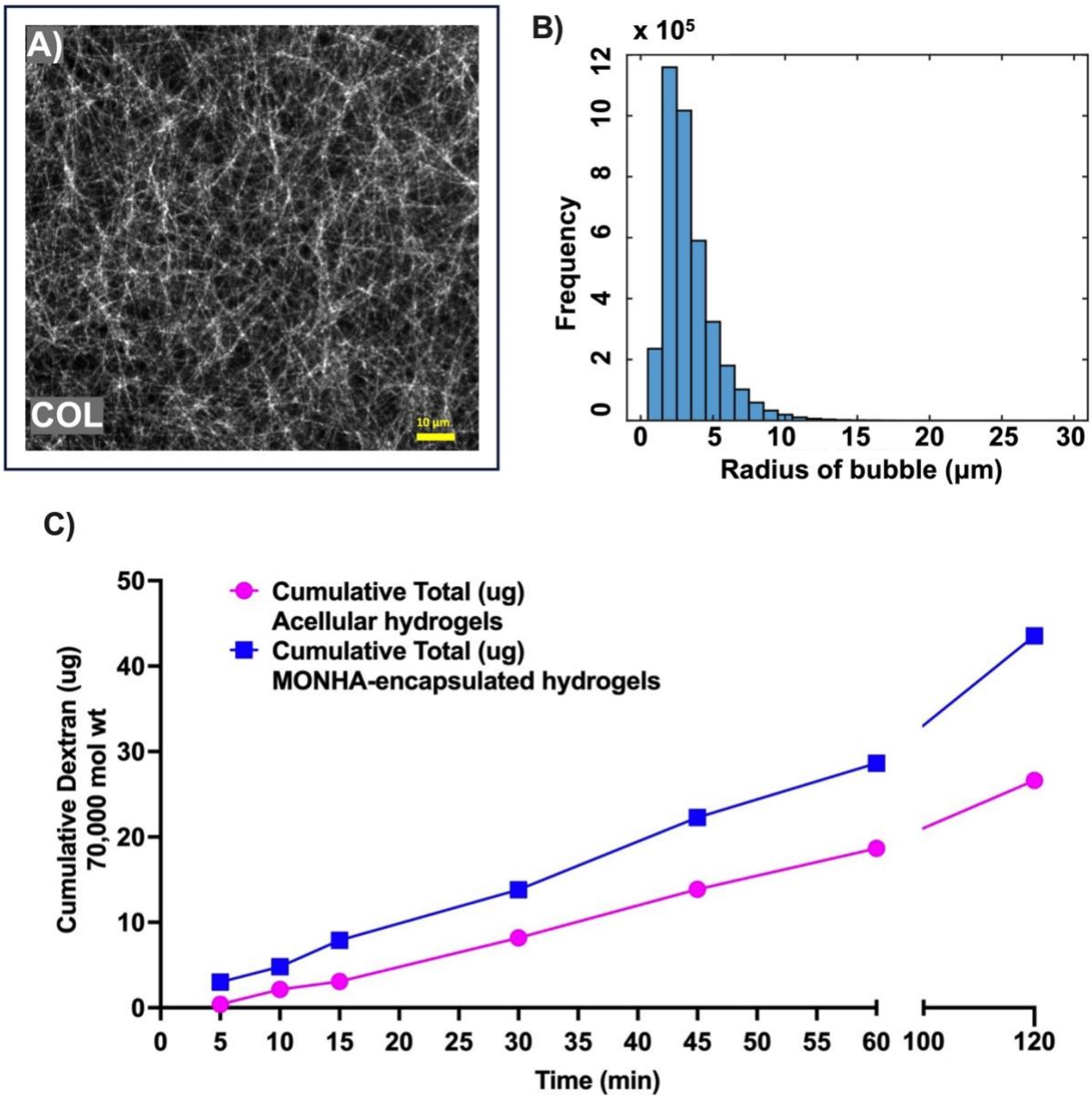

199

200 **Supplemental Fig. 1. Characterization of the MONHA-encapsulated ECM hydrogel model.**
201 **(A)** Representative fluorescence image of collagen fibril distribution and **(B)** quantification of pore
202 size within acellular hydrogels (N = 5 hydrogels). Scale bar 10 µm. **(C)** Assessment of the
203 normalized average permeability of acellular and MONHA-encapsulated hydrogels (N = 3
204 hydrogels/group) as calculated by FITC-labelled 70kDa dextran as tracer molecule.
205

To characterize the architecture of the ECM network within our MONHA-encapsulated hydrogels, we evaluated the compaction of collagen fibrils. We observed regional differences within our constructs such that samples at baseline (under no biomechanical strain) displayed increased collagen compaction in the periphery of the ECM hydrogel as compared to the core (Suppl. Fig 2A-B). Moreover, the collagen compaction appeared greater immediately adjacent to astrocyte cell bodies/processes (Suppl. Fig. 2A). Collectively, these data support that encapsulated ONH astrocytes differentially remodel and contract their surrounding collagen fibers in the core as compared to the unbound periphery of the hydrogel. Because of this heterogeneity in collagen compaction, we artificially delineated the core from the periphery of MONHA-encapsulated hydrogels for subsequent experiments and comparisons (Suppl. Fig. 2C).

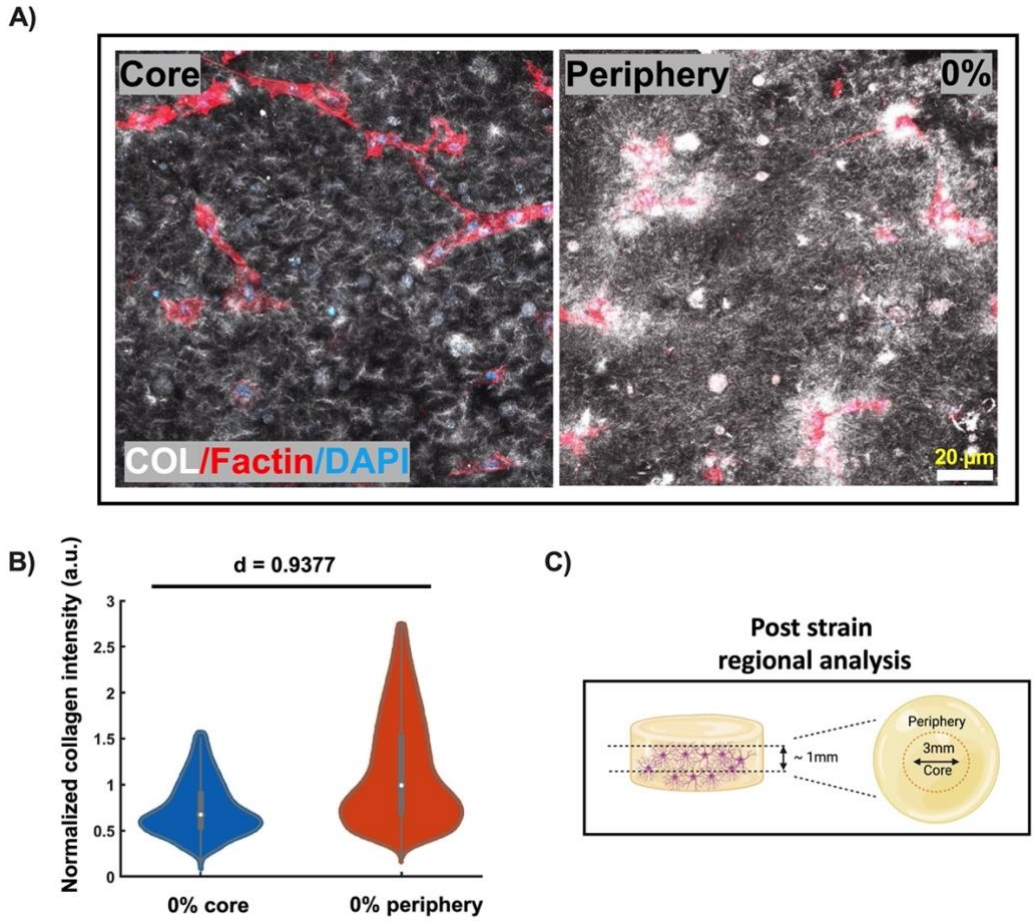

Supplemental Fig. 2. Regional differences in collagen fibril compaction of MONHA-encapsulated hydrogels. (A) Density of collagen fibrils in the core and periphery of the MONHA-encapsulated hydrogels after 2 weeks in culture; scale bar 20 µm. **(B)** Quantitative analysis of normalized collagen compaction within the core and periphery of MONHA-encapsulated hydrogels (N = 3 hydrogels/group). Cohen's d = 0.20, 0.50, and 0.80 is used to indicate the effect sizes as small, medium, or large, respectively. **(C)** Schematic delineating regional segmentation of MONHA-encapsulated hydrogels post biomechanical strain.

2.2 Quantification of astrocyte cell viability within MONHA-encapsulated hydrogels after compressive strain

After characterizing the ECM hydrogel, we then applied compressive biomechanical strains to MONHA-encapsulated hydrogels using a custom bioreactor [23-25]. We used 3% and 10% compressive strains at a frequency of 1 Hz, which have been reported in ONH tissues during glaucomatous insult [18-20]. After 24h compression, we quantified astrocyte cell viability in MONHA-encapsulated hydrogels (Suppl. Fig. 3). We found no detectable difference in total viability by MTS assay after compression for 24h (Suppl. Fig. 3).

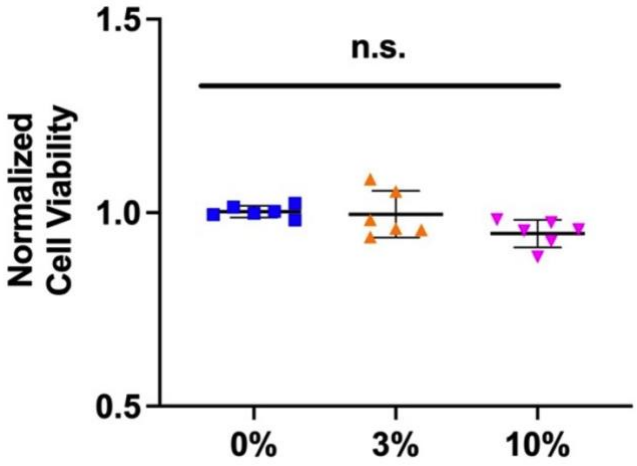

Supplemental Fig. 3. Cell viability following compressive strain. Normalized MONHA cell viability after 24h compression via MTS assay (N = 6 hydrogels/group). Significance was determined by one-way ANOVA using multiple comparisons tests.

240 ***2.3 Compressive strain alters MONHA cytoskeletal architecture***

241 Immediately following glaucomatous insult, ONH astrocytes *in situ* respond by reorienting
242 their cell bodies and remodeling their F-actin cytoskeleton architecture [12-14, 27]. Thus, we asked
243 whether isolated compressive strains would induce similar F-actin and cytoskeletal reorganization.
244 To do so, we quantified F-actin area coverage and levels of GFAP expression in MONHA-
245 encapsulated hydrogels after biomechanical strain application for 4h and 24h, respectively.

246 After 4h compression, MONHAs showed no significant changes in F-actin area coverage
247 in either the core or periphery of the ECM hydrogels (Fig. 1A-C). In contrast, after 24h
248 compression, there was a significant drop in F-actin area coverage within the core of the hydrogel
249 in a strain-dependent manner (Fig. 1A-C). Both 3% and 10% groups showed ~50% decrease in F-
250 actin area coverage compared to control (0%) (Fig. 1C), which was also associated with increased
251 cell alignment in the 10% compression group (Suppl. Fig. 4A,B). Interestingly, application of
252 compressive strain did not alter the F-actin area coverage or cell alignment in the periphery of the
253 ECM hydrogel in either strain group (Fig. 1C; Suppl. Fig. 4C,D). Overall, these data demonstrate
254 that encapsulated MONHAs are robustly mechanoresponsive, altering cellular morphology in
255 response to biomechanical stimuli.

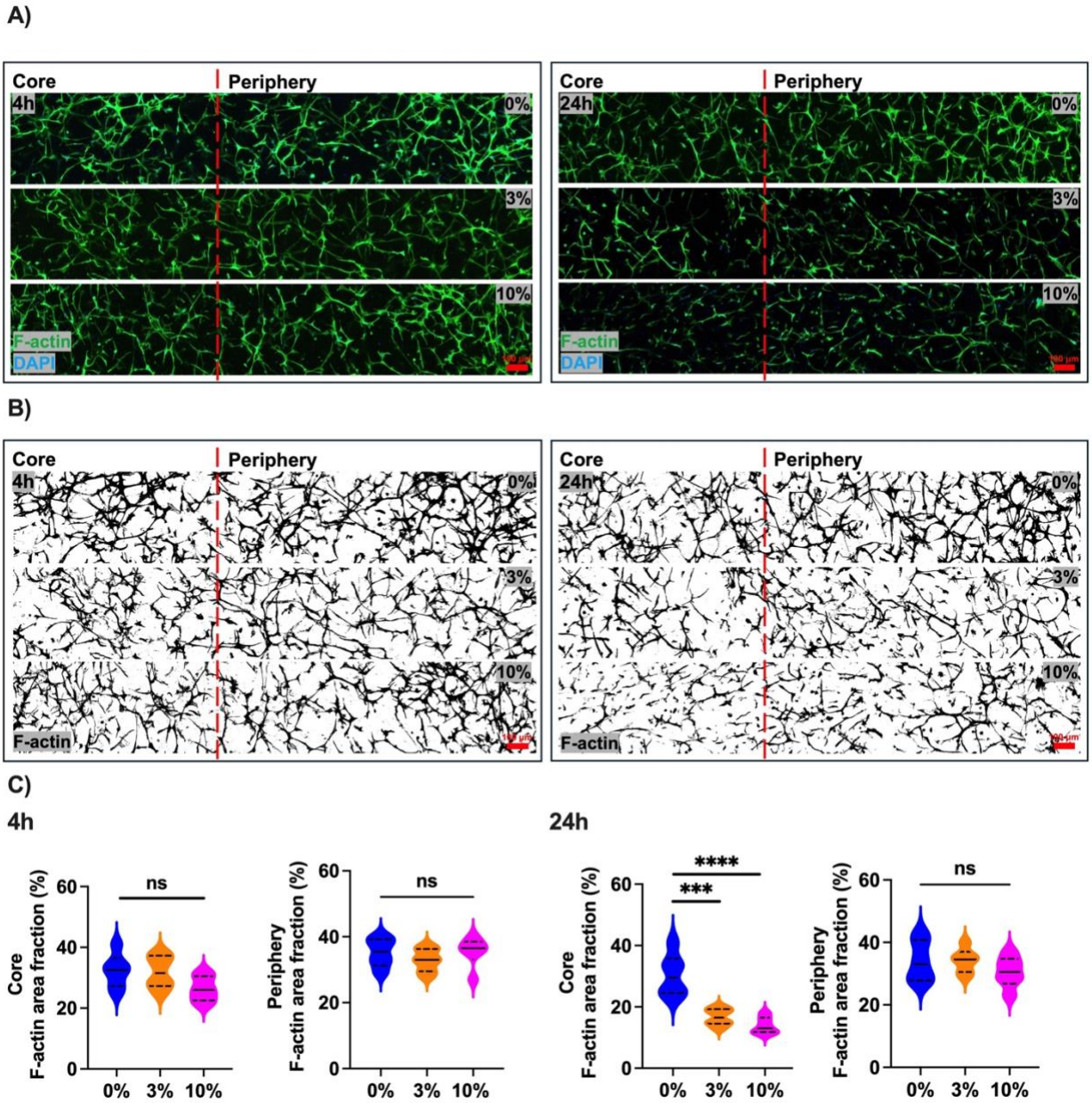

Fig. 1. Regional differences in MONHA morphology in response to duration and magnitude of compressive strain. (A) Representative fluorescence images of astrocyte F-actin staining (A) and cytoskeletal binarized masks (B). Scale bar: 100 µm. **(C)** Quantitative analyses of F-actin mask area (n = 6 fields of view/group collected from N = 2-3 hydrogels/group). Statistical significance was determined using one-way ANOVA (*p < 0.05 , **p < 0.01, ***p < 0.001, **** p < 0.0001) for F-actin area fraction analyses.

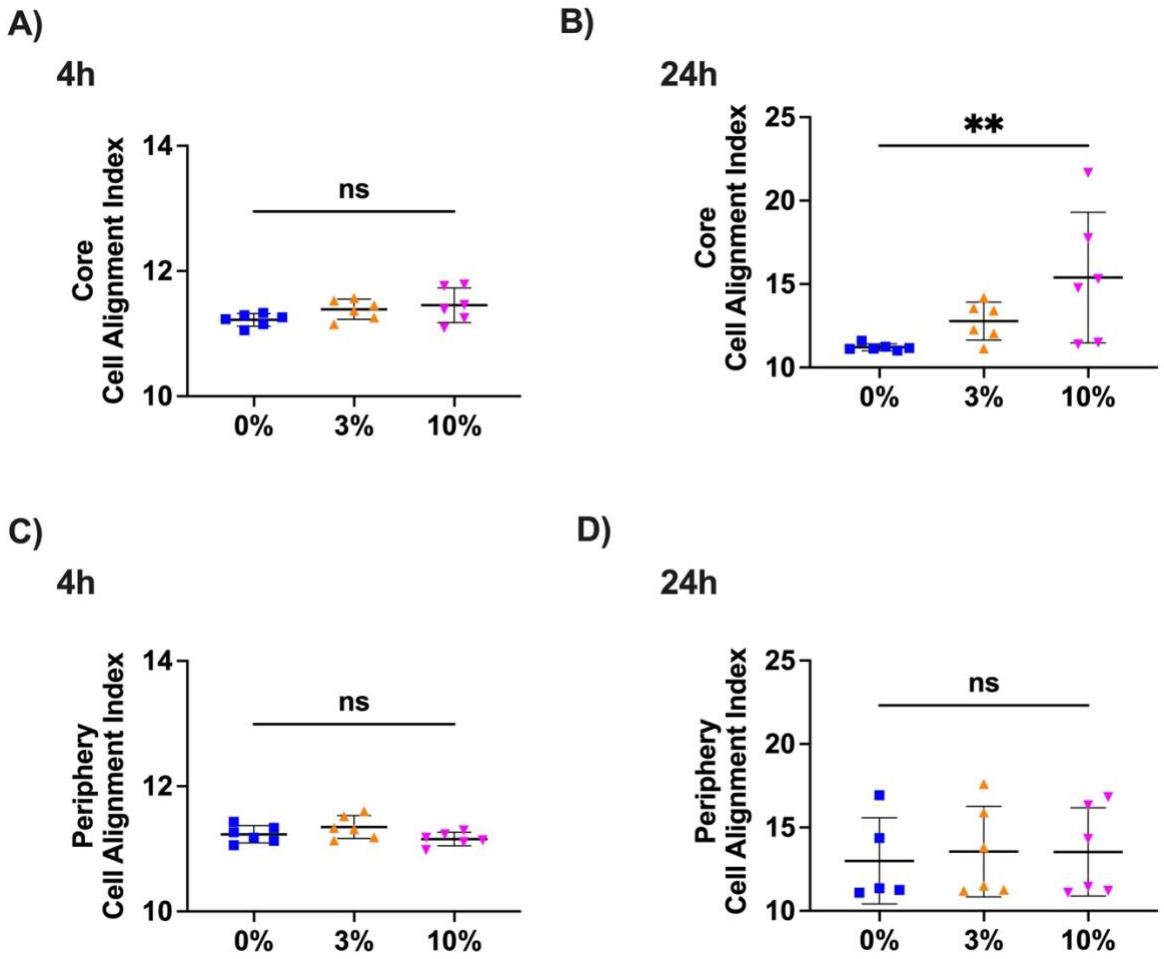

Supplemental Fig. 4. Regional differences in encapsulated MONHA cell alignment in response to compressive strain. Quantitative analyses of cell alignment based on F-actin mask area (n = 5-6 fields of view/group collected from N = 3 hydrogels/group) in response to 4h **(A)** and 24h of increasing biomechanical strain (i.e., 3% or 10%) **(B)** within the core of the hydrogel, and 4h **(C)** and 24h of biomechanical strain **(D)** within the periphery of the hydrogel, Statistical significance was determined using one-way ANOVA (** $p < 0.01$).

Astrocytes respond to glaucomatous insults within the ONH by undergoing reactive gliosis, in part characterized by an increase in expression of intermediate filaments such as GFAP [30, 31]. We previously showed that both MONHAs in 2D and encapsulated within 3D ECM hydrogels can be induced to express higher levels of GFAP upon stimulation with a known inducer of astrocyte reactivity such as exogeneous TGFβ2 [22, 32]. Therefore, we asked whether application of compressive strain would induce a similar induction in intermediate filaments. Control (0%

compression) MONHA-encapsulated hydrogels showed baseline immunoreactivity of GFAP throughout the hydrogel. After both 4h and 24h compression, GFAP immunolabeling increased ~1.5-fold in both the core and periphery of the ECM hydrogel (Fig. 2A-C, Suppl. Fig. 5A-C). As such, these data support that compressive strains directly induce cytoskeletal alterations in encapsulated astrocytes.

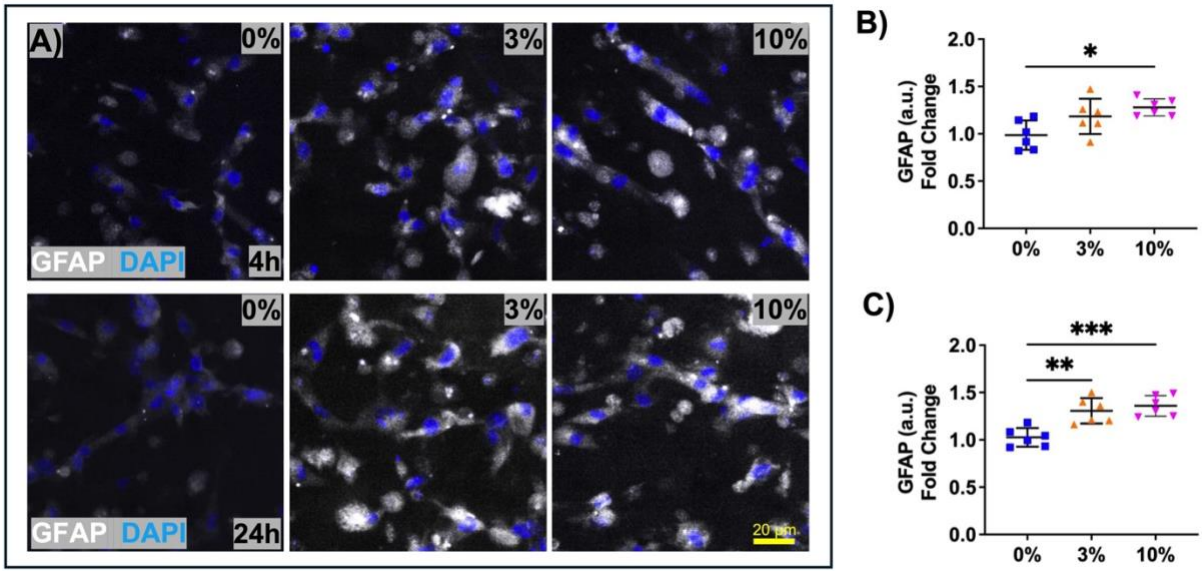

Fig. 2. GFAP expression of encapsulated-MONHAs within the hydrogel core in response to compressive strain. (A) Representative fluorescence images and quantification of fold change in astrocyte GFAP signal intensity (n = 6 fields of view/group collected from N = 3 hydrogels/group) after **(B)** 4h and **(C)** 24h of increasing strain (i.e., 3% or 10%). Statistical significance was determined using one-way ANOVA (*$p < 0.05$, **$p < 0.01$, ***$p < 0.001$) for GFAP expression levels. Scale bar: 20 µm.

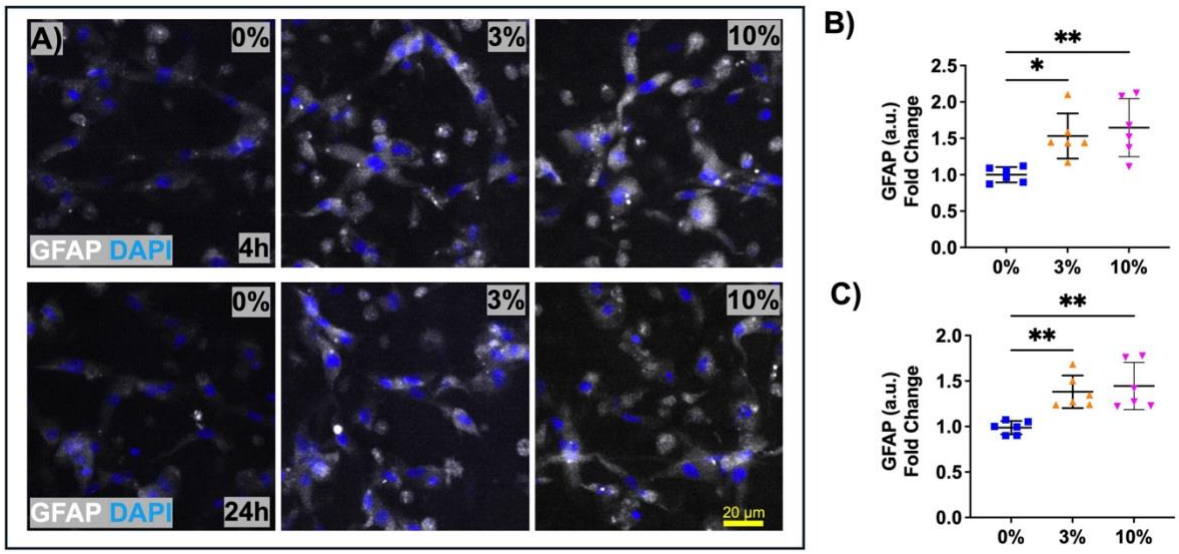

Supplemental Fig. 5. GFAP expression of encapsulated-MONHAs within the hydrogel periphery in response to compressive strain. (A) Representative fluorescence images and quantification of fold change in astrocyte GFAP signal intensity (n = 6 fields of view/group collected from N = 3 hydrogels/group) after **(B)** 4h and **(C)** 24h of increasing strain (i.e., 3% or 10%). Statistical significance was determined using one-way ANOVA (*$p < 0.05$, **$p < 0.01$) for GFAP expression levels. Scale bar: 20 µm.

2.4 Compressive strain alters HIF-1α levels within MONHA-encapsulated hydrogels

Glaucomatous insults are associated with hypoxia and metabolic stress within the retina and ONH since IOP-induced deformations can impact the local vasculature and reduce tissue oxygenation [33, 34]. Thus, we asked if astrocytes within our model could modulate expression of hypoxia-inducible factor (HIF), thereby potentially affecting downstream metabolic activity. Specifically, to determine whether encapsulated MONHAs undergo such metabolic stress in response to biomechanical strain, we examined levels of HIF-1α after application of compressive strain. HIF-1α immunoreactivity was low in control (0%) samples at both timepoints (i.e., 4h and 24h; Fig. 3, Suppl. Fig. 6) regardless of ECM hydrogel region (i.e., core vs periphery). Hydrogel-encapsulated MONHAs exhibited significantly increased HIF-1α levels by ~1.25-fold in the core groups after 4h compression and by ~2-fold in the periphery (Fig. 3A, B); HIF-1α also increased

312 ~1.5-2-fold after 24h compression (Fig. 3A, C). Similar trends of HIF-1α elevation were observed
313 in the periphery of the ECM hydrogel (Suppl. Fig. 6). Taken together, these data support that
314 compressive strain can directly induce changes in metabolic regulatory factors.
315

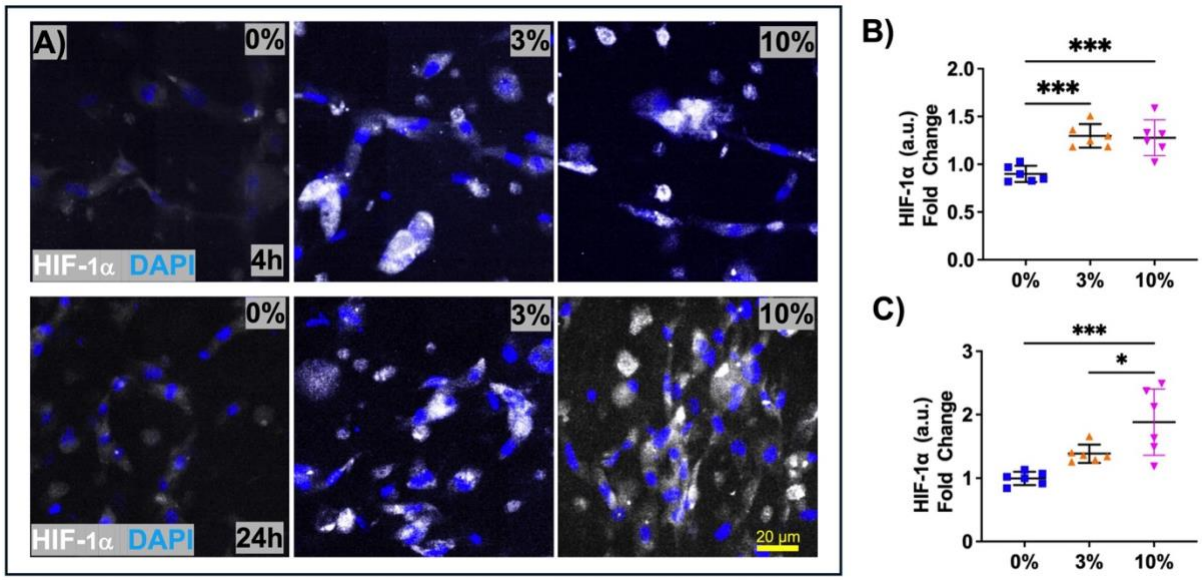

316

317 **Fig. 3. HIF-1α expression of encapsulated-MONHAs within the hydrogel core in response to**
318 **compressive strain. (A)** Representative fluorescence images and quantification of fold change in
319 astrocyte HIF-1α expression signal intensity (n = 6 fields of view/group collected from N = 3
320 hydrogels/group) after **(B)** 4h and **(C)** 24h of increasing strain (i.e., 3% or 10%). Statistical
321 significance was determined using one-way ANOVA (*$p < 0.05$, **$p < 0.01$, ***$p < 0.001$) for
322 HIF-1α expression levels. Scale bar: 20 µm.
323

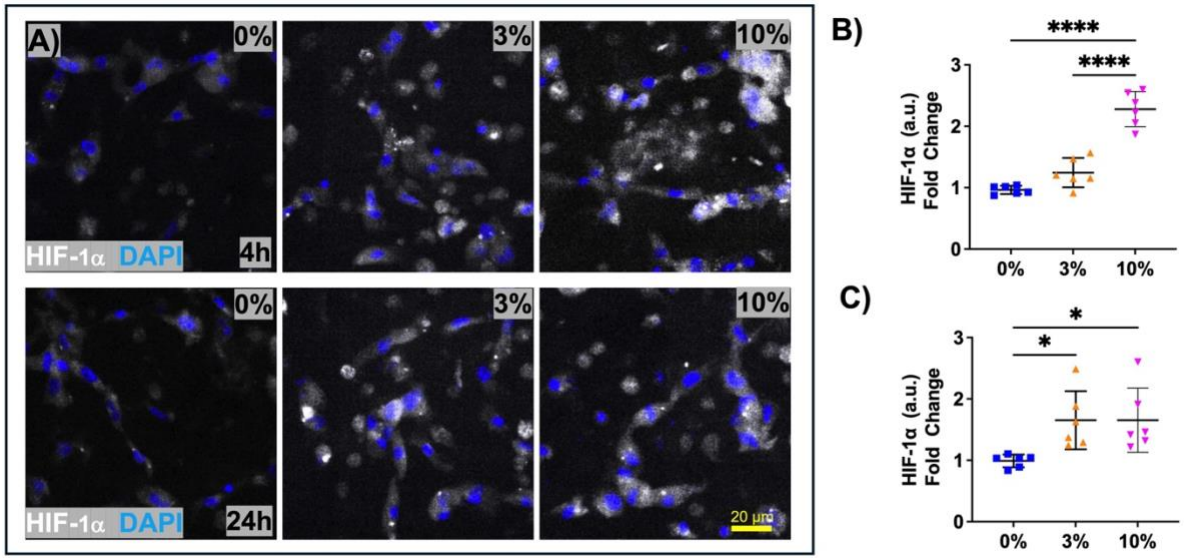

Supplemental Fig. 6. HIF-1α expression of encapsulated-MONHAs within the hydrogel periphery in response to compressive strain. (A) Representative fluorescence images and quantification of fold change in astrocyte HIF-1α expression signal intensity (n = 6 fields of view/group collected from N = 3 hydrogels/group) after **(B)** 4h and **(C)** 24h of increasing strain (i.e., 3% or 10%). Statistical significance was determined using one-way ANOVA (*$p < 0.05$, **** $p < 0.0001$) for HIF-1α expression levels. Scale bar: 20 µm.

2.5 Compressive strain on MONHA-encapsulated hydrogels induces matrix remodeling via collagen network remodeling and fibronectin deposition

In situ, ONH astrocytes modulate their surrounding ECM via secretion of crosslinking and/or degrading enzymes [15, 30]. Therefore, we asked how application of compressive strain would influence astrocyte modulation of the ECM microenvironment within our hydrogels. We first performed confocal reflectance microscopy to directly visualize collagen fibers within MONHA-encapsulated hydrogels after compression. We previously showed that control constructs (0%) display regional differences in collagen arrangement, with more uniformly distributed collagen fibers within the core of the ECM hydrogel, and an increased density of collagen fibers in the periphery of the hydrogel (Suppl. Fig. 2). While 4h compression did not induce significant remodeling of the collagen fibrils across groups, after 24h compression, both 3% and 10% showed significant *decrease* of collagen compaction within the core (Fig. 4A, B) and

345 a significant *increase* in collagen compaction in the periphery compared to control (0%) (Suppl.
346 Fig. 7A, B). Collectively, these data support that application of compressive strain for 24h
347 significantly alters collagen compaction within ECM hydrogels in a region-dependent manner.

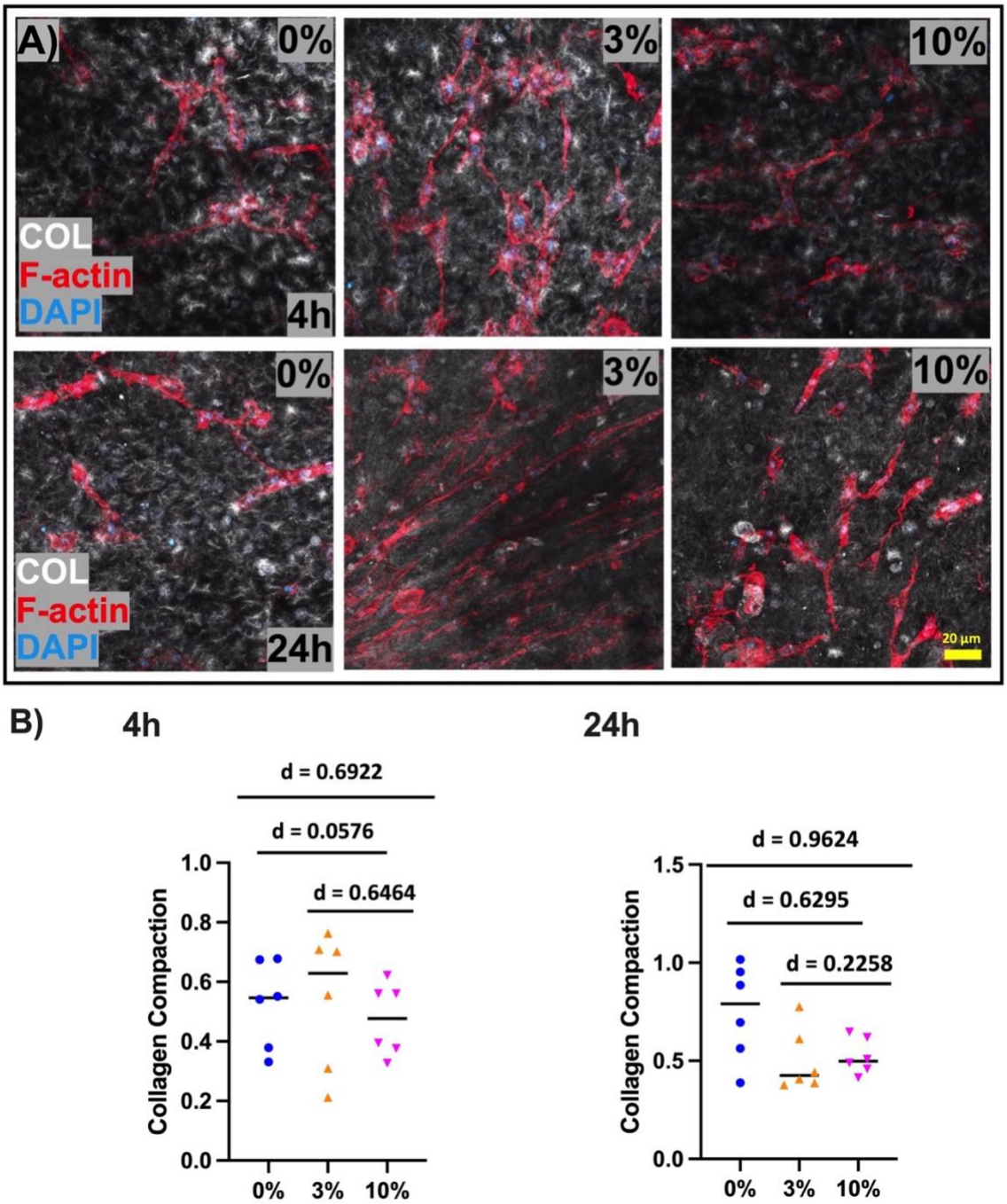

348

349 **Fig. 4. ECM collagen fibrils remodeling in the core of MONHA-encapsulated hydrogels in**
350 **response to compressive strain. (A)** Representative fluorescence images of collagen fibrils

remodeling in response to duration (i.e., 4h or 24h) and magnitude of strain (i.e., 3% or 10%) (n = 6 fields of view/group collected from N = 3 hydrogels/group). Scale bar: 20 µm. **(B)** Quantification of collagen compaction after compression. Cohen's effect size d (Cohen's d = 0.20, 0.50, and 0.80 is used to indicate the effect sizes as small, medium, or large, respectively).

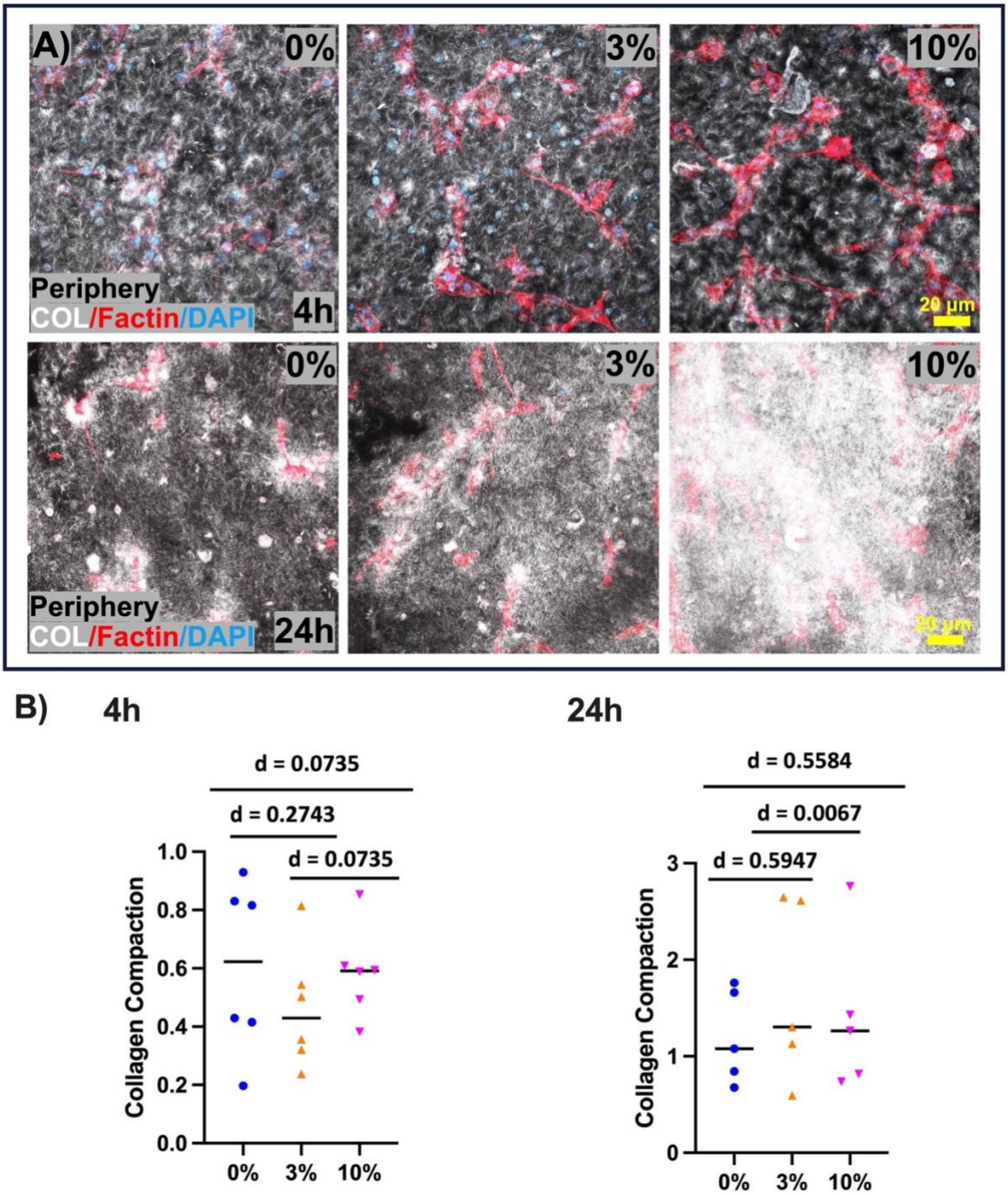

Supplemental Fig. 7. ECM collagen fibrils remodeling in the periphery of MONHA-encapsulated hydrogels in response to compressive strain. (A) Representative fluorescence images of collagen fibrils remodeling in response to duration (i.e., 4h or 24h) and magnitude of strain (i.e., 3% or 10%) (n = 5-6 fields of view/group collected from N = 3 hydrogels/group). Scale bar: 20 µm. **(B)** Quantification of collagen compaction after compression. Cohen's effect size d (Cohen's d = 0.20, 0.50, and 0.80 is used to indicate the effect sizes as small, medium, or large, respectively).

Reactive astrocytes increase secretion of key ECM scaffold proteins such as fibronectin. This glycoprotein can also interact with other ECM proteins (i.e., collagen I and laminin) further promoting matrix crosslinking and, thus, contribute to the stiffening and fibrosis of the ONH tissue [15, 35, 36]. As such, we investigated how compressive strain impacts astrocyte secretion of fibronectin. Across all groups, strain increased fibronectin deposition in MONHA-encapsulated hydrogels (Fig. 5). After 4h compression, hydrogels showed a ~2.5-3-fold increase in fibronectin immunolabeling within the core, and a ~1.5-fold increase within the periphery (Fig. 5 A, B). Similar trends were observed with 24h compression, such that the core displayed a ~6-fold increase (Fig. 5 A, C), and the periphery of the ECM hydrogels had a less robust ~2-fold increase in fibronectin immunolabelling (Suppl. Fig. 8).

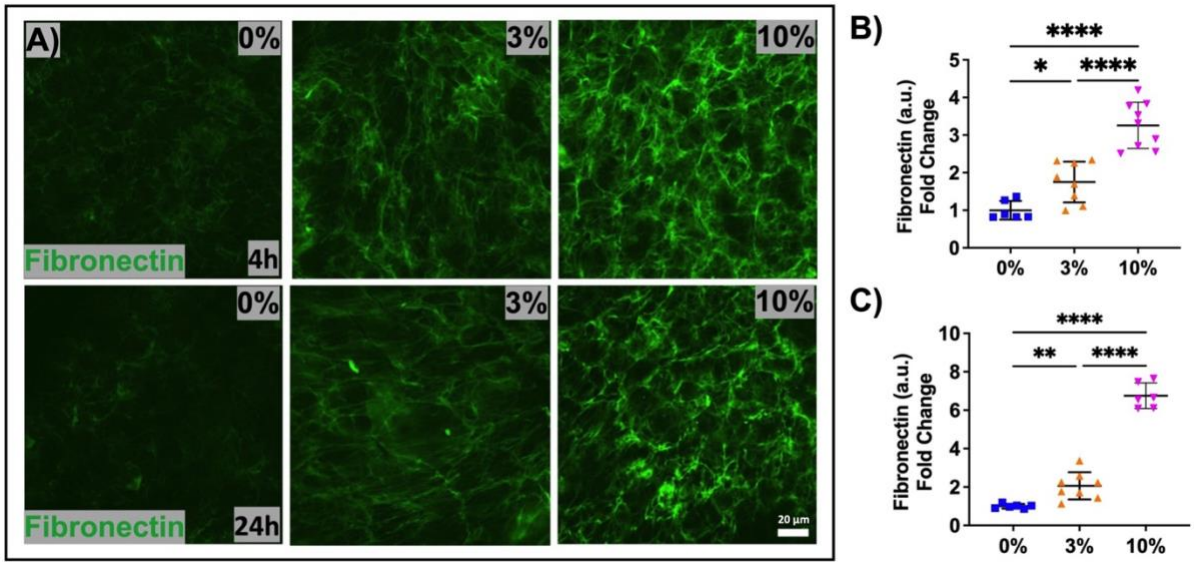

Fig. 5. Fibronectin levels in the core of MONHA-encapsulated hydrogels in response to compressive strain. (A) Representative fluorescence images of fibronectin in response to duration

(i.e., 4h or 24h) and magnitude of strain (i.e., 3% or 10%) (n = 6-9 fields of view/group collected from N = 3 hydrogels/group) and **(B-C)** quantification of fold change in fibronectin signal intensity. Statistical significance was determined using one-way ANOVA (*p < 0.05 , **p < 0.01, **** p < 0.0001) for fibronectin signal intensity. Scale bar: 20 µm.

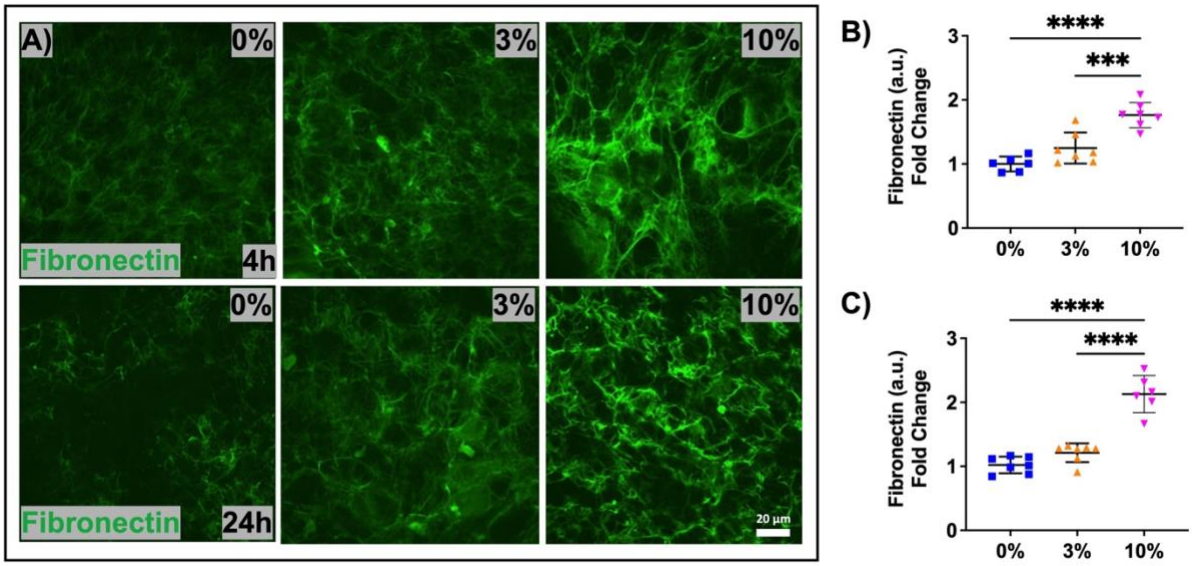

Supplemental Fig. 8. Fibronectin levels in the periphery of MONHA-encapsulated hydrogels in response to compressive strain. (A) Representative fluorescence images of fibronectin in response to duration (i.e., 4h or 24h) and magnitude of strain (i.e., 3% or 10%) (n = 6-7 fields of view/group collected from N = 3 hydrogels/group) and **(B-C)** quantification of fold change in fibronectin signal intensity. Statistical significance was determined using one-way ANOVA (***p < 0.001, **** p < 0.0001) for fibronectin signal intensity. Scale bar: 20 µm.

The observed alterations in ECM protein compaction and deposition could potentially impact the global stiffness of MONHA-encapsulated hydrogels. Thus, we analyzed the overall rheological properties of hydrogels after compressive strain. After application of 3% or 10% compression for 24h, we found no significant differences in hydrogel stiffness compared to their uncompressed (0%) controls (Suppl. Fig. 9).

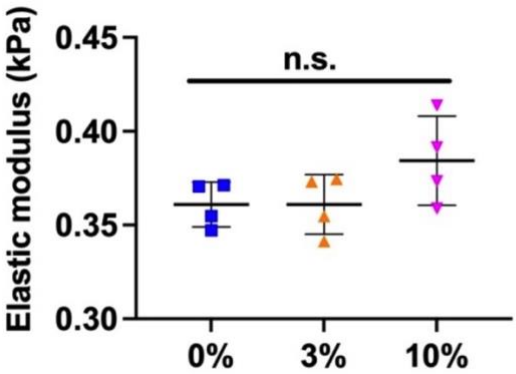

Supplemental Fig. 9. MONHA-encapsulated hydrogel stiffness following compressive strain. Analysis of the elastic modulus (kPa) of MONHA-encapsulated hydrogels (N = 4 hydrogels/group) following 24h compression (i.e., 3% or 10%). Significance was determined by one-way ANOVA using multiple comparisons test.

Collectively, these data show that compressive strain significantly alters collagen distribution and astrocyte fibronectin production in MONHA-encapsulated hydrogels, indicating a dynamic interplay between mechanical stimuli, ECM remodeling, and astrocyte mechanoresponse.

2.6 Compressive strain regulates global transcriptomic response of MONHAs across strain level and time

Astrocytes within the ONH are transcriptionally responsive to alterations in IOP. Several murine experimental glaucoma studies have investigated the effects of elevated IOP on ONH astrocyte gene expression and downstream responses [37, 38]. However, it is not clear how glaucoma-associated *biomechanical strains* directly affect ONH astrocyte gene expression and molecular pathways. Given the robust phenotypic response to compressive strain, we next investigated the transcriptional response of ONH astrocytes to compression across strain intensities and durations. Overall, all the RNA samples showed high quality indicated by an RNA integrity number (RIN) ≥ 8.

To assess the global transcriptional effects of compression on astrocytes, we performed principal component analysis (PCA) on bulk RNA sequencing data from MONHA-encapsulated hydrogels subjected to 0%, 3%, or 10% compression for either 4 hours or 24 hours per ECM hydrogel region (i.e., core or periphery). PCA revealed that the duration of compression primarily drove transcriptional variation, with samples separating along PC1 (Suppl. Fig. 10A, B). Strain dynamics in both regions were most observed with 10% strain revealing an initial significant shift along PC2 and PC3 in the 4h groups and maintained in 24h groups.

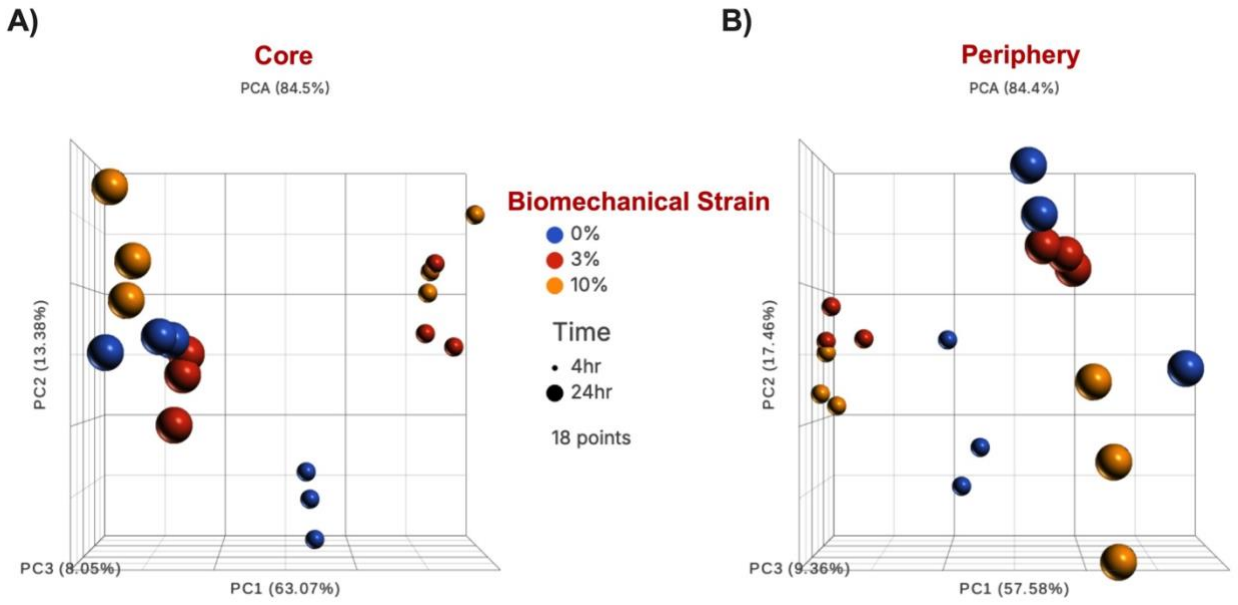

Supplemental Fig. 10. Regional principal component analyses of encapsulated MONHAs transcriptomes in response to compressive strain over time. Each point represents an individual replicate per region (n = 18/core and 18/periphery) subjected to compression (blue = 0%, red = 3%, orange = 10%) for 4 hours (small spheres) or 24 hours (large spheres). Duration of strain (i.e., time) is the dominant source of variation, with point separation along PC1, and magnitudes of strain are observed with PC2 and PC3. **(A)** In the core region, the three principal components (i.e., PC1: 63.07%, PC2: 13.38%, PC3: 8.05%) collectively explain 84.5% of the total variance. **(B)** In the periphery, the three principal components (i.e., PC1: 57.58%, PC2: 17.46%, PC3: 9.36%) account for 84.4% of total variance.

438 ***2.7 Pairwise analysis reveals distinct transcriptional responses dependent on magnitude of***
439 ***compressive strain and hydrogel region***

440 We next analyzed how different compressive strain intensities (i.e., 3% or 10%) affect
441 MONHA gene expression at different timepoints (i.e., 4h or 24h). DESeq2 analysis identified
442 19,163 genes after 4h compression and 18,376 genes after 24h compression. We applied a cutoff
443 of FDR ≤ 0.05 and fold change |FC| ≥ 1.5. DEGs from the core of the hydrogel are depicted in
444 Table 1 and in Fig. 6 A, B and Fig. 7 A, B. To simplify the discussion, we have annotated groups
445 by "magnitude of strain" followed by "hydrogel region"; thus, the ECM hydrogel core that
446 underwent 3% biomechanical strain is denoted as *3c*, while the hydrogel periphery is denoted as
447 *3p*. In response to both intensities of biomechanical strain, we observed fewer DEGs in the 24h
448 group vs the 4h group, supporting that encapsulated MONHAs adapt to compressive strain with
449 increasing durations (Table 1).

	4h	24h
3% vs 0%	**1,368 total DEGs** 686 upregulated, 682 downregulated	**377 total DEGs** 104 upregulated; 273 downregulated
10% vs 0%	**1,968 total DEGs** 880 upregulated; 1088 downregulated	**413 total DEGs** 147 upregulated; 266 downregulated

450 **Table 1.** DEGs with FDR ≤ 0.05 and fold change |FC| ≥ 1.5, core of the hydrogel.

451 For all groups, to identify the functional categories the DEGs were enriched in, the list of
452 DEGs per comparison were uploaded to the publicly available WEB-based GEne SeT AnaLysis
453 platform. In the *3c* group after 4h compression, over representation analysis (ORA) revealed
454 enrichment of GOs involved in cell-cell junction, collagen-containing ECM, laminin/fibronectin
455 binding, and cell proliferation and migration (Fig. 6C). With increased magnitude of strain, the
456 *10c* group after 4h compression showed enriched pathways in the regulation of immune/defense
457 response, response to cytokine, mitochondrion, adenosine triphosphate (ATP)/nucleotide binding,
458 and regulation of programmed cell death (Fig. 6D). These findings suggest that, for relatively short

459 durations (i.e. 4h), increasing the magnitude of compressive strain induced a shift in DEGs
460 enriched in morphology, ECM regulation, and cell proliferation (3%) to enrichment in
461 inflammation regulating and cell cycle/division-related pathways (10%) (Fig. 6C, D).

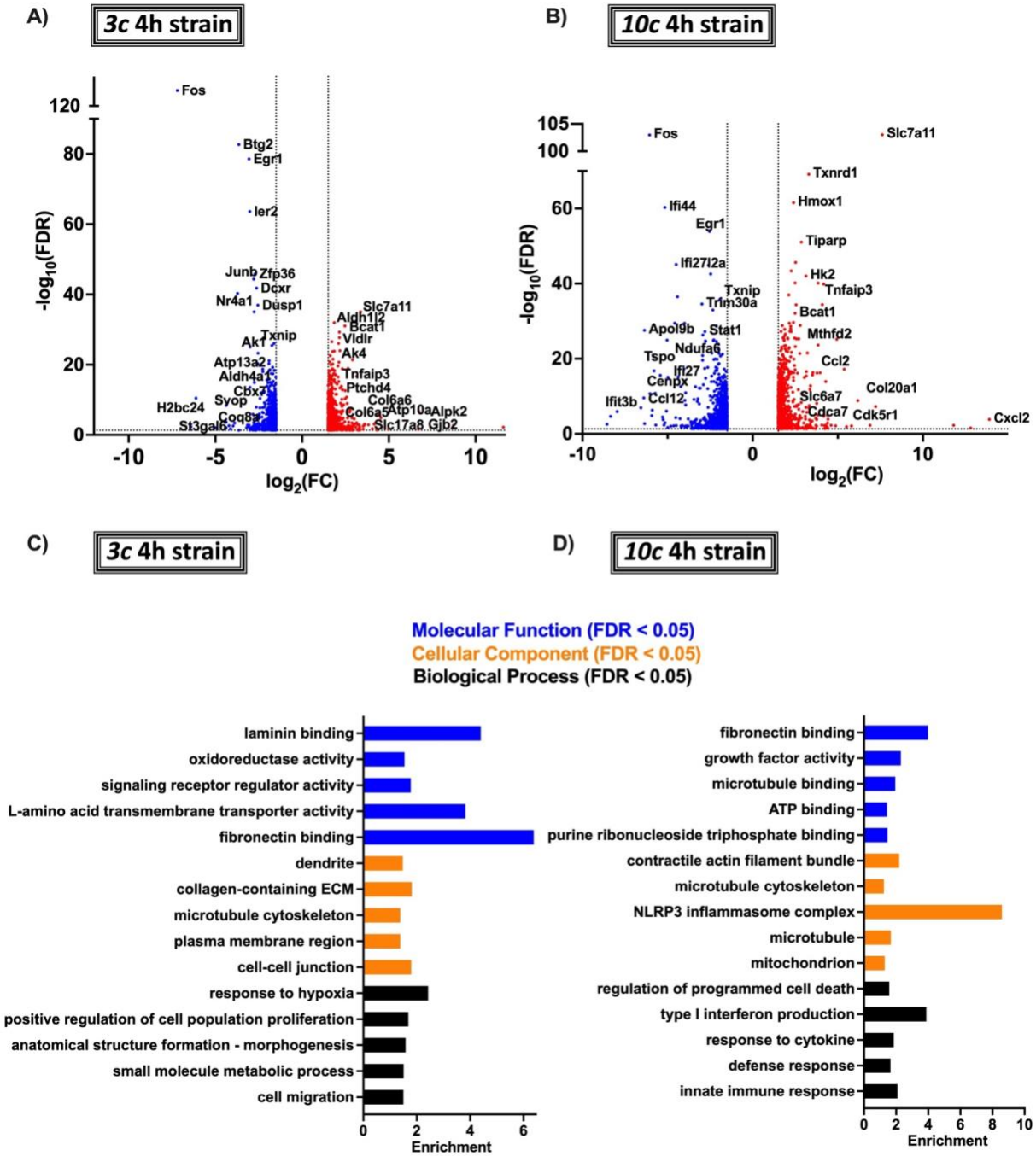

462

463 **Fig. 6. Pairwise transcriptional mechanoresponse of MONHAs encapsulated within the**
464 **hydrogel core to 4h of compressive strain. (A-B)** Volcano plots representing the number of

465 DEGs with FDR ≤ 0.05 and |FC| ≥ 1.5 in response to 3% and 10% compression for 4h. **(C-D)**
466 Listed are five representative gene ontology (GO) pathways per functional group of the top 30
467 most significant GOs at each timepoint.
468
469
470 Similar analyses were done for MONHAs undergoing compressive strain for 24h. For the
471 *3c* group after 24h compression, GOs showed genes enriched in cell cycle, DNA replication,
472 organelle fission, condensed chromosome, microtubule associated complex, DNA helicase activity
473 and ATP binding (Fig. 7C). In contrast, in the *10c* group after 24h compression, GOs showed
474 enriched genes in pathways of carbohydrate/AMP binding, response to hormone, cell–substrate
475 junction, response to hypoxia, and oxidoreductase activity (Fig. 7D). These findings suggest that
476 application of compressive strain for longer durations (24h) induces a shift in DEGs enriched cell
477 cycle and division pathways (3%) to enrichment in metabolism and ECM regulatory pathways
478 (10%) (Fig. 7C, D).
479

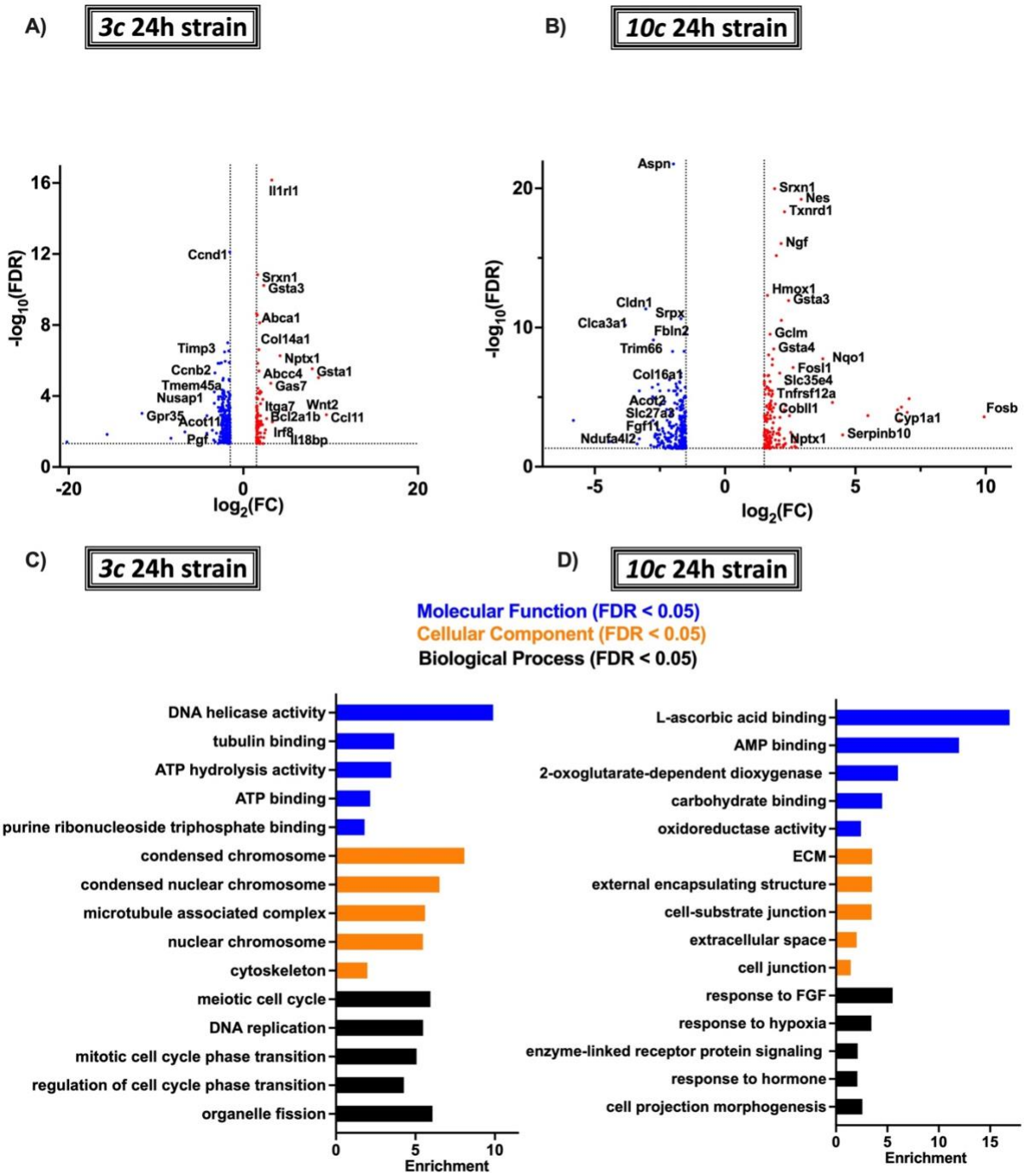

Fig. 7. Pairwise transcriptional mechanoresponse of MONHAs encapsulated within the hydrogel core to 24h of compressive strain. (A-B) Volcano plots representing the number of DEGs with FDR ≤ 0.05 and |FC| ≥ 1.5 in response to 3% and 10% biomechanical strain for 24h. **(C-D)** Listed are five representative gene ontology (GO) pathways per functional group of the top 30 most significant GOs at each timepoint.

487 We then analyzed the periphery of the hydrogel, where cells were surrounded by more
488 densely packed ECM (Suppl. Fig. 2). Again, we applied a cutoff of FDR ≤ 0.05 and fold change
489 |FC| ≥ 1.5; DEGs from the periphery of the hydrogel are depicted in Table 2 and in Suppl. Fig. 11
490 A, B and Suppl. Fig. 12 A, B.

	4h	24h
3% vs 0%	**688 total DEGs** 336 upregulated, 352 downregulated	**13 total DEGs** 6 upregulated; 7 downregulated
10% vs 0%	**801 total DEGs** 322 upregulated; 479 downregulated	**445 total DEGs** 112 upregulated; 333 downregulated

491 **Table 2.** DEGs with FDR ≤ 0.05 and fold change |FC| ≥ 1.5, periphery of the hydrogel.

492

493 In this peripheral region, for relatively short duration compression (4h), we similarly
494 observed that MONHAs displayed a shift in DEGs enriched in cellular signaling regulation (*3p*)
495 to inflammation and metabolism pathways (*10p*) (Suppl. Fig. 11C, D). Interestingly, analysis of
496 the *3p* group after 24h compression identified few DEGs with no significant GOs by our FDR
497 cutoff values. The *10p* group after 24h compression showed GOs primarily enriched in ECM
498 regulation and adhesion (Suppl. Fig. 12C). Taken together, these transcriptomic analyses reveal
499 that astrocytes exhibit highly dynamic time– and region–dependent transcriptional responses to
500 compressive strain, transitioning from early changes in signaling, inflammation and metabolism
501 to later changes in matrix remodeling and adhesion.

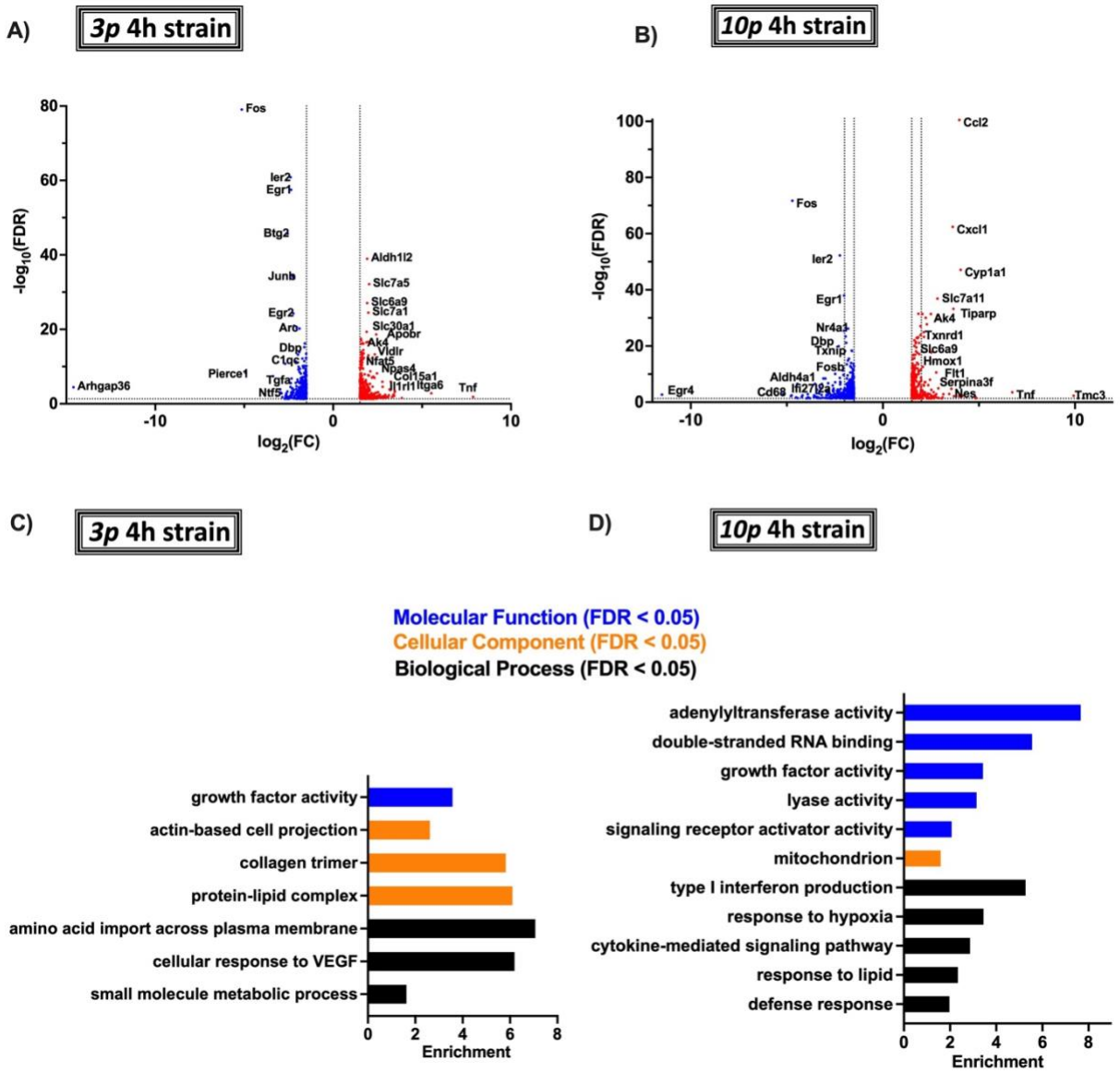

Supplemental Fig. 11. Pairwise transcriptional mechanoresponse of MONHAs encapsulated within the hydrogel periphery to 4h of compressive strain. (A-B) Volcano plots representing the number of DEGs with FDR ≤ 0.05 and |FC| ≥ 1.5 in response to 3% and 10% biomechanical strain for 24h. **(C)** Listed are up to five representative gene ontology (GO) pathways per functional group of the top 30 most significant GOs after 4h of strain.

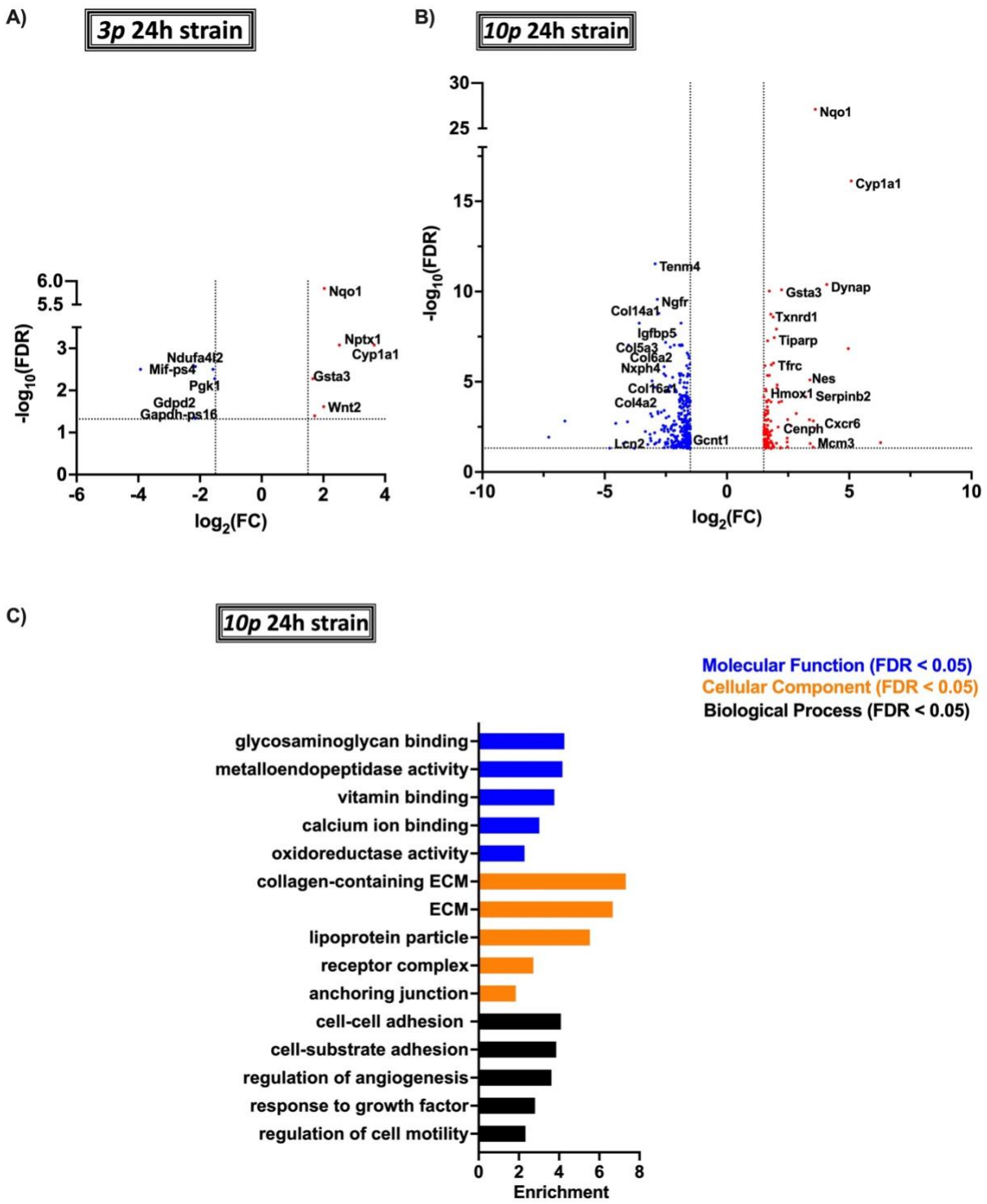

Supplemental Fig. 12. Pairwise transcriptional mechanoresponse of MONHAs encapsulated within the hydrogel periphery to 24h of compressive strain. (A-B) Volcano plots representing the number of DEGs for 24h with FDR ≤ 0.05 and |FC| ≥ 1.5 in response to 3% and 10% biomechanical strain for 24h. **(C)** Listed are five representative gene ontology (GO) pathways per functional group of the top 30 most significant GOs at each timepoint.

515 ***2.8 Hydrogel region and duration of compressive strain modulate key astrocytic molecular and***
516 ***metabolic pathways***

517 To investigate the contribution of increasing magnitude and duration of compression to
518 MONHA transcriptional response, we performed ANOVA of compressive strain groups across
519 timepoints followed by GSEA against both KEGG and Reactome databases. In the hydrogel core,
520 encapsulated astrocytes downregulated pathways related to focal adhesions (*Col6a6; Flnc; Flt1;*
521 *Hgf; Itga10*), integrin cell surface interactions (*Itga5; Itga7; Itgb3; Itgb8; Lama2*), and ECM
522 interactions (*Col6a5; Col6a6; Itga10; Tnxb*) (Fig. 8A, B, D). These altered pathways corroborate
523 our findings on genes enriched in GOs associated with cell morphology and ECM reorganization.
524 Compressive strain on ECM hydrogel-encapsulated astrocytes also led to the downregulation of
525 key signaling pathways regulating astrocyte quiescence, including those regulating stem cell
526 pluripotency (*Rest; Tbx3; Wnt11*), calcium signaling (*Camk2a; Fzd3; Fzd4*), interleukin-6 (IL6)
527 (*Clcf1; Cntfr; Il6ra; Lif; Lifr; Osmr*), phosphoinositide 3-kinase Ak strain transforming (PI3K-
528 Akt) (*Bcl2l11; Chuk; Vegfa; Flt3l; Gdnf; Hgf; Il6ra*), and Wnt signaling (*Wnt11; Wnt5a*) (Fig.
529 8A, B, D).

530 Additionally, MONHAs encapsulated within the core of the ECM hydrogel showed
531 significant changes in metabolism with increasing time and magnitude of compression.
532 Specifically, we observed upregulated pathways related to metabolic and respiratory electron
533 transport chain (ETC) (Fig. 8A, B, C). As a part of the mitochondrial oxidative phosphorylation,
534 the ETC is crucial for ATP production. These upregulations corresponded with gene enrichment
535 in metabolism/ETC complexes and in thermogenesis (*Acot2; Aldh1a1; Acy1; Adh7; Atp6v0d2;*
536 *Cox6b1; Cox7a2; Cox7b; Cox7c; Cox8a; Ndufa1; Ndufa11; Ndufa12; Ndufb8*) (Fig. 6A-C).
537 Interestingly, pathways for both cell cycle/repair (*Ccnb1; Ccnb2; Ccne1; Cdc20; Cdc45; Cdk1;*

538 *Cdk18; Chek2*) and cellular senescence (*Ccna2; Ccne2; Foxm1; Map2k6; Rbl1; Rras*) were also
539 upregulated (Fig 8A-C), potentially indicating a cytoprotective stress response to increasing
540 biomechanical strain over time.

541 We then investigated the hydrogel periphery, where astrocytes were surrounded by a denser
542 ECM at baseline. Interestingly, we observed a somewhat blunted transcriptional response to
543 compressive strain in the periphery with fewer DEGs (Table 2) identified compared to the core of
544 the hydrogel (Table 1). Similarly to the core region, peripheral MONHAs downregulated pathways
545 related to inflammation such as IL17–signaling, cytokine–cytokine receptor interaction (*Lif; Cntfr;*
546 *Il11; Il1r1*) as well as signaling pathways implicated in astrocyte quiescence like stem cell
547 pluripotency, calcium or PI3K-Akt/Wnt signaling (*Nfatc2; Tnxb; Vegfa; Wnt2; Wnt5a*) (Suppl.
548 Fig. 13A-D). Importantly, unlike the core, we observed a larger number of significant molecular
549 pathways upregulated in cell cycle, mitosis, DNA synthesis, replication, and repair, ATP activation
550 in response to replication stress, and chromosome maintenance (*Ccnb2; Cdc20; Atp6v0d2;*
551 *Cox6b1; Ndufa1; Cox6b1; Mcm3*) (Suppl. Fig. 13A-D). As such, the astrocytes within the ECM
552 hydrogel periphery exhibit a distinct shift toward pathways supporting proliferation, DNA
553 maintenance, and replication stress responses. Collectively, these findings show that compressive
554 strain plays a crucial role in shaping astrocyte morphology, function, and ECM regulation
555 concomitant with a robust mechanotranscriptional response.

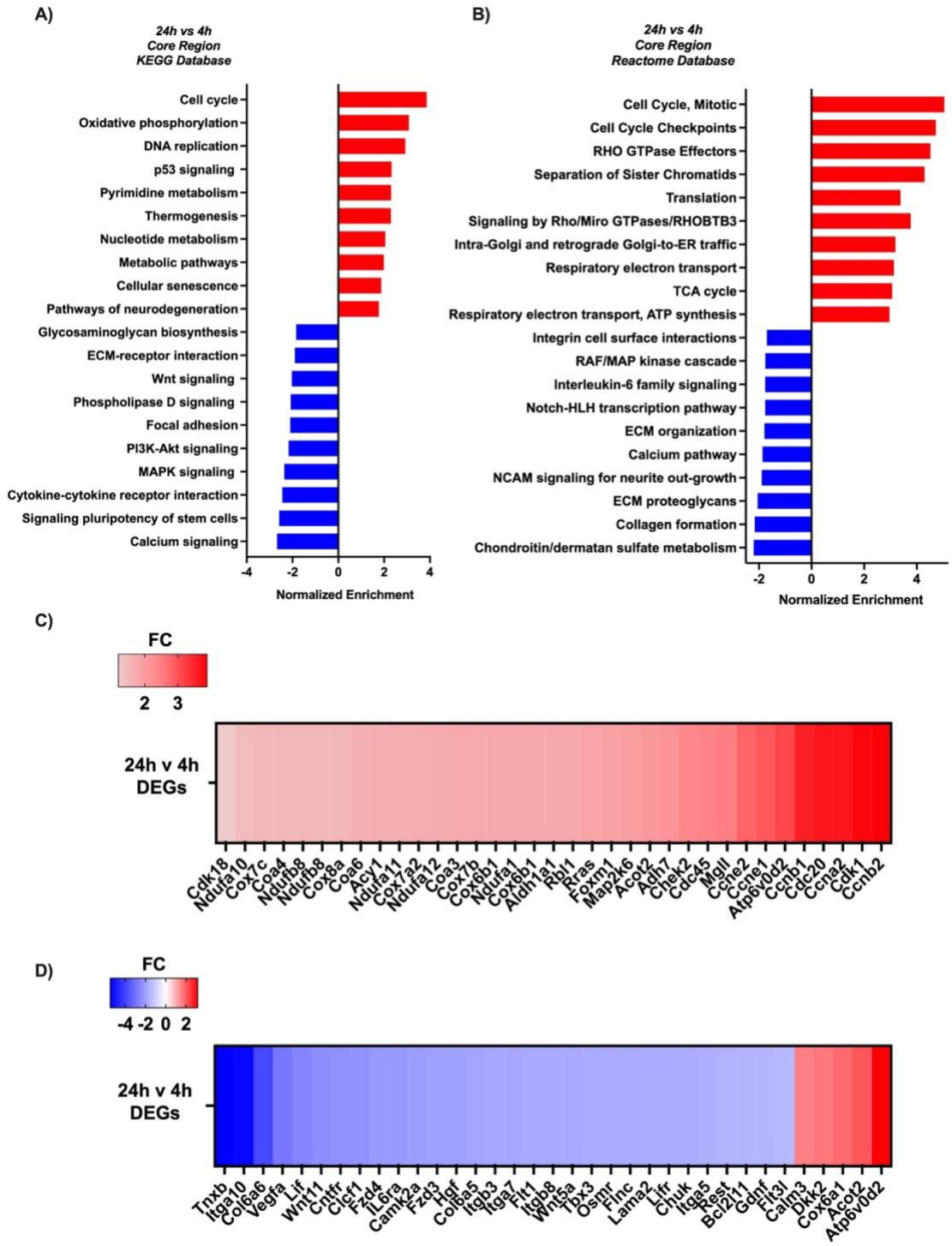

556

557 **Fig. 8. Transcriptional mechanoresponse of MONHAs encapsulated within the hydrogel**
558 **core over time with increasing compressive strain intensity and duration. (A-B)** Listed here
559 are 20 up and down most significant pathways against KEGG and Reactome databases with
560 representative 35 DEGs for the **(C)** upregulated and **(D)** downregulated pathways (FDR ≤ 0.05

561 and |FC| ≥ 1.5) based on ANOVA analysis of MONHAs mechanoresponse over time (i.e., 24h vs
562 4h) with increasing strain.

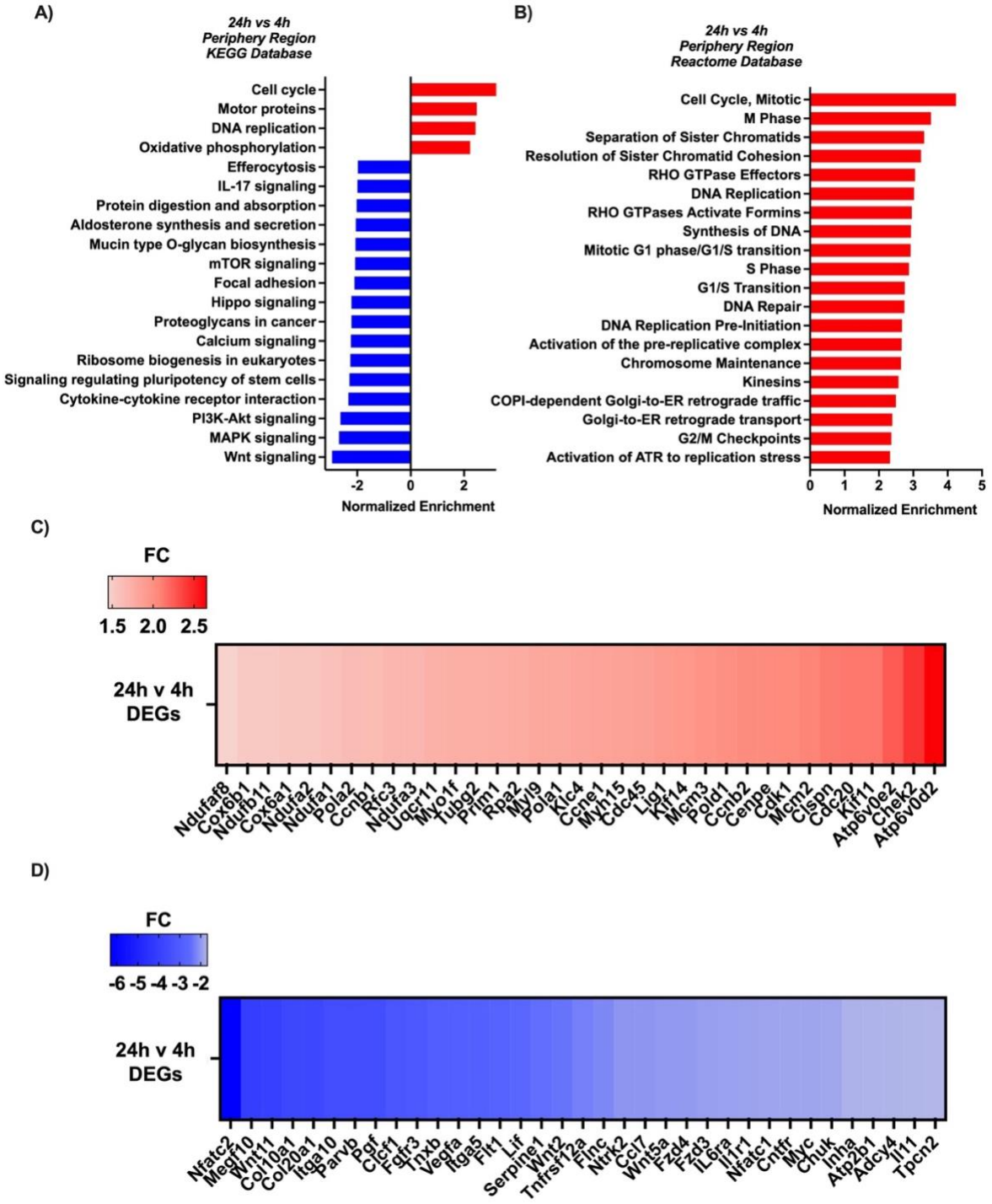

563

564 **Supplemental Fig. 13. Transcriptional mechanoresponse of MONHAs encapsulated within**
565 **the hydrogel periphery over time with increasing compressive strain intensity and**
566 **duration. (A-B)** Listed here are 20 up and down most significant pathways against KEGG and

567 Reactome databases with representative 35 DEGs for the **(C)** upregulated and **(D)** downregulated
568 pathways (FDR ≤ 0.05 and |FC| ≥ 1.5) based on ANOVA analysis of MONHAs
569 mechanoresponse over time (i.e., 24h vs 4h) with increasing strain.

570

571 ***3. Discussion***

572 In glaucoma, increased biomechanical strains on the ONH have long been associated with
573 elevated IOP and disease progression [18-20, 30]; and yet, the mechanoresponse of ONH resident
574 cells remains poorly understood. ONH astrocytes have emerged as key regulators of retinal
575 ganglion cell axonal health. In *in vivo* glaucoma models, these local astrocytes are amongst the
576 first to respond by reorganizing their cytoskeleton architecture and gap junction coupling [12-14,
577 27, 39]. In the present study, we sought to comprehensively analyze the direct phenotypic and
578 transcriptional responses of astrocytes to glaucomatous biomechanical strains, to better understand
579 the role of these pathologic biomechanical forces on astrocyte behavior.

580

581 ***Dissecting the ONH astrocyte mechanoresponse by modeling glaucomatous compressive strains***
582 ***in a 3D ECM hydrogel***

583 Prior studies explored ONH astrocyte mechanoresponse to glaucomatous biomechanical
584 strains using conventional 2D *in vitro* cultures [17, 40]. However, it is increasingly recognized that
585 the ECM significantly influences cell behavior, with mechanical, structural, and compositional
586 cues playing critical roles [41]. Newer *in vitro* 3D models, including our own [22], utilize
587 viscoelastic ECM biopolymer hydrogels made from collagen and hyaluronic acid to better mimic
588 the 3D architecture and promote a more natural astrocyte morphology [6, 41, 42]. By encapsulating
589 astrocytes within a collagen/hyaluronic acid network, one can directly visualize cell–cell and cell–
590 ECM interactions. We previously showed that hydrogel-encapsulated murine ONH astrocytes

591 extend processes in 3D, couple with astrocyte neighbors, and bind to and modify their surrounding
592 ECM [22]. In this study we sought to comprehensively investigate how 3D-encapsulated ONH
593 astrocytes respond to glaucoma-related compressive strains over time. A custom bioreactor
594 previously used on collagen-encapsulated rat cortical astrocytes [23], was used to apply increasing
595 intensities of compressive strain over time to investigate nuanced ONH astrocyte phenotypic and
596 transcriptomic responses to mechanical stimuli.
597
598 ***Compressive strain triggers a multifaceted phenotypic and transcriptomic response in***
599 ***encapsulated astrocytes, mimicking aspects of glaucomatous ONH astrocyte dysfunction***
600 Four main astrocyte mechanoresponses were observed in this study. After compression,
601 MONHAs demonstrated alterations in (i) cell division/senescence, (ii) cytoskeletal architecture
602 and morphology, (iii) ECM remodeling, and (iv) metabolic function. These findings are largely in
603 line with ONH astrocyte behavior in *in vivo* glaucoma models, and highlight the potentially
604 instrumental role of glaucomatous compressive strains in regulating ONH dysfunction. Our
605 finding of robust transcriptional alterations related to cell cycle regulation and DNA replication
606 suggests development of a proliferative and/or senescent phenotype in MONHAs following
607 compression. Early in *in vivo* glaucoma models, ONH astrocytes proliferate, and exhibit increased
608 reactive gliosis [11, 39, 43]. With prolonged IOP elevation, ONH astrocytes show evidence of cell
609 senescence and death [44, 45]. Interestingly, in our study, transcriptional alterations did not
610 correlate with altered astrocyte viability in response to relatively short durations of compressive
611 strain (i.e., 4h and 24h), suggesting that longer durations compressive strain are necessary to
612 induce astrocyte senescence/death in 3D *in vitro*.

613 One of the most profound findings in our study was a robust change in F-actin cytoskeleton
614 architecture after compressive strain. In the core of the ECM hydrogel, there was a significant
615 decrease in F-actin area coverage, suggestive of MONHA process retraction that correlated with
616 increasing intensity and duration of compression. We also observed downregulated pathways of
617 focal adhesion and ECM-interactions, and significant GOs pertaining to cytoskeleton, actin–based
618 cell projection, dendrite and cell–cell junction. This is particularly interesting in light of *in vivo*
619 evidence that ONH astrocytes undergo a dramatic reorientation of their F-actin cytoskeleton within
620 8 – 72 h of acute IOP elevation [10, 13, 14, 39], and a decrease in astrocyte process complexity
621 and coupling [27, 44]. These early morphologic changes in ONH astrocytes may reduce astrocyte–
622 astrocyte connectivity as well as contact with surrounding blood vessels, retinal ganglion cell
623 axons, and ECM, potentially propagating glaucomatous damage.

624 Moreover, the observed morphologic alterations corresponded with reorganization of the
625 surrounding ECM. After 24h compression, there was a significant reduction in collagen
626 compaction surrounding MONHAs in the core of the hydrogel, suggesting that the changes in F-
627 actin area coverage may diminish cell–ECM interactions, thereby hindering their ability to remodel
628 surrounding collagen fibrils. We also observed increased fibronectin levels and significant
629 enrichment of genes associated with collagen, fibronectin, and ECM modulation. This response of
630 MONHAs to pathologic compressive strain aligns with the behavior of ONH astrocytes *in vivo*; in
631 glaucoma, astrocytes modify the ECM extensively, leading to increased ECM protein (such as
632 fibronectin) production and crosslinking [15, 30, 35, 36, 46, 47].

633 A key feature of the glaucomatous ONH is the dysregulation of metabolic pathways [30,
634 31, 39, 48, 49]. Within 4h compression, there was increased HIF-1α expression, which can trigger
635 transcription of hypoxia–responsive genes, affecting downstream metabolism [34, 50, 51].

636 Simultaneously, sequencing revealed enrichment of genes involved in cell response to hypoxia
637 pathways, which persisted at longer durations (24h). We also observed upregulated metabolic and
638 respiratory electron transport/ATP synthesis pathways with genes enriched in mitochondrion and
639 ATP binding. In glaucoma models, the optic nerve undergoes hypoxia and metabolic insufficiency,
640 correlating with increased glycolysis and ATP production [34, 52-54]. In response to compressive
641 strain, we observed similar early (within 4h) alteration in pathways related to hypoxia and oxygen
642 levels.

643 We were surprised to find certain divergent phenotypes in the periphery of the ECM
644 hydrogel when compared to the core. In the periphery, F-actin area coverage and cellular/process
645 morphology remained unchanged after compressive strain, and we observed a surrounding
646 *increase* in collagen compaction. Additionally, while compressive strain resulted in gene
647 enrichment in cell cycle and numerous ECM regulatory pathways (similar to the astrocytes
648 residing in the core), there was greater gene enrichment in metabolic pathways such as
649 mitochondrion, vitamin binding, small metabolic process, oxidoreductase activity, and response
650 to growth factors. Notably, there were numerous pathways upregulated in cell cycle/stress,
651 oxidative phosphorylation and organelle protein trafficking, and downregulated
652 reactivity/inflammation. At baseline (prior to application of compressive strain), this peripheral
653 region was characterized by increased collagen compaction (Suppl. Fig. 2). It is possible that a
654 denser ECM in the hydrogel periphery may dampen the pro-inflammatory astrocyte phenotype,
655 while increasing cell cycle and metabolic alterations. *In vivo*, acute IOP elevation is associated
656 with significant alteration in metabolism-related genes in ONH astrocytes, with a relatively muted
657 inflammatory response [37, 55]. This aligns with our compression injury-induced *in vitro* model.
658 The regional differences in phenotypic and transcriptomic responses by hydrogel-encapsulated

659 astrocytes highlight the important role that ECM integrity plays in regulating astrocyte response
660 to biomechanical strain.
661
662 ***Limitations and future directions***
663 The presented *in vitro* ECM hydrogel model provides evidence for compressive
664 biomechanical strain injury as a driving force in ONH astrocyte pathophysiology in glaucoma.
665 While astrocyte mechanoresponse was largely consistent throughout the hydrogel, there were a
666 few regional differences observed. Potential reasons for this variability include baseline
667 differences between the core and periphery of the hydrogel, such as the baseline ECM compaction
668 (as evidenced in Suppl. Fig. 2), relative differences in biomechanical strain profile across regions,
669 and variable oxygen concentration within the ECM hydrogel. Finite element modeling of the strain
670 profile experienced throughout the unconfined hydrogel using this compression bioreactor
671 predicted a relatively uniform compressive strain distribution [24], but the contribution of regional
672 variations in tensile and shear strain is unknown. It is also possible that large hydrogels (i.e., 8 x 4
673 mm constructs) have decreased oxygen concentration in the core as compared to the periphery of
674 the hydrogel. However, we observed prompt tracer diffuse through the hydrogel (Suppl. Fig. 1),
675 suggesting that cells in the core of the ECM hydrogel have adequate access to media nutrients.
676 Additionally, greater gene enrichment regulating metabolic processes were observed in the
677 periphery of the hydrogel compared to the core, where one would expect relatively higher oxygen
678 concentration.
679 Here, we encapsulated MONHAs in a relatively simplified fibrillar ECM hydrogel, which
680 does not precisely recapitulate the complex composition of a primate lamina cribrosa nor a murine
681 astrocytic lamina [35, 56]. In the future, the hydrogel could be modified by ECM patterning, to

682 generate a more representative lamina cribrosa–like structure. Many of our insights into
683 mechanisms of glaucoma pathophysiology are gained from experimental rodent models [12, 26,
684 27, 37, 57]. Building on this foundation, we encapsulated *murine* ONH astrocytes to compare and
685 contrast to the *in vivo* findings. Furthermore, by isolating and precisely controlling application of
686 biomechanical strain, we established a platform to directly dissect the specific contribution of
687 compressive strain to astrocyte mechanoresponses. Our model system does allow for the
688 incorporation of other resident cells, including human ONH cell types or microglia, enabling
689 analysis of different cell–cell interactions under biomechanical strain. Compressive strains of 3%
690 and 10% were selected based on finite element modeling predictions of the strains experienced by
691 the glaucomatous ONH [19, 23, 58, 59], and 1Hz was selected to mimic the cyclic ocular pulse
692 amplitude [60]. Future studies can modify superimposed strain and frequency dependent on the
693 species of origin (i.e., murine cells vs. human cells).
694
695 ***Conclusions***
696 Glaucoma is a complex multifactorial neurodegeneration, for which pathologic
697 biomechanical strain is a key driving factor in ONH pathology. By encapsulating astrocytes from
698 the tissue of interest (i.e., the ONH) within a biologically-relevant ECM hydrogel, we have
699 comprehensively defined the contribution of these compressive strains to ONH astrocyte behavior.
700 As the key mechanosensors of the ONH, astrocytes are critical for initiating complex molecular
701 cascades that can result in both protective and detrimental outcomes, underscoring the importance
702 of studying their nuanced mechanoresponse.
703
704

705 ***4. Methods***

706 ***4.1 Mouse ONH astrocyte isolation and culture***

707 C57BL/6J mice were purchased from the Jackson Laboratory (Bar Harbor, ME) and bred
708 in house according to the institutional guidelines for the humane treatment of animals (IACUC
709 #473) and to the ARVO Statement for the Use of Animals in Ophthalmic and Vision Research.
710 Each harvest used 5-8 mice aged 6-8 weeks. The isolation/culture of primary mouse ONH
711 astrocytes (MONHAs) was performed as previously described [32]. Briefly, optic nerve head
712 tissue was dissected from each eye using a SMZ1270 stereomicroscope at a location proximal to
713 the sclera. The samples then underwent digestion in 0.25% trypsin (Invitrogen, 25200-056,
714 Carlsbad, CA, USA) for 15 minutes at 37 °C. Following digestion, the tissue was resuspended in
715 MONHA growth medium, consisting of Dulbecco's modified Eagle's medium, DMEM/F12
716 (Invitrogen, 11330-032, Grand Island, NE, USA), supplemented with 10% fetal bovine serum
717 (FBS; Atlanta Biologicals, S11550, Atlanta, GA, USA), 1% penicillin/streptomycin (Corning, 30-
718 001-CI, Manassas, VA, USA), 1% Glutamax (Invitrogen, 35050-061, Grand Island, NY, USA),
719 and 25 ng/ml epidermal growth factor (EGF; Sigma, E4127-5X, St. Louis, MO, USA). The
720 digested ONH tissue was then plated onto T75 cell culture flasks coated with 0.2% gelatin and
721 incubated at 37 °C in a humidified atmosphere with 5% CO2. MONHAs migrated from the ONH
722 tissue over a period of 10-14 days before the first passage. All subsequent experiments included
723 MONHAs at passage 3.

724

725 ***4.2 Preparation of PDMS molds***

726 A polydimethylsiloxane (PDMS) mixture was used at a 10:1 ratio of elastomer to curing
727 agent as per the manufacturer's instructions (PDMS; Sylgard 184, Dow Corning, Midland, MI,

728 USA). This mixture was poured into custom 3D printed ABS-M30 filament negative molds (F170;
729 Stratasys, Eden Prairie, MN, USA), measuring either 10 mm diameter x 6 mm depth or 8 mm
730 diameter x 4 mm depth, cured at 60°C, and autoclaved prior to use.
731
732 ***4.3 Preparation of MONHA-encapsulated ECM hydrogels***
733 MONHA-encapsulated hydrogels were prepared as previously described [22]. Briefly,
734 MONHAs (2.5×10^6 cells/ml) in media were mixed with 3.1 mg/ml methacrylate-conjugated
735 bovine collagen type I (MA-COL; molecular weight: ~300 kDa, degree of methacrylation: ~60–
736 70%; Advanced BioMatrix, Carlsbad, CA, USA), 1 mg/ml thiol-conjugated hyaluronic acid (SH-
737 HA; Glycosil®; molecular weight: ~300 kDa, degree of thiolation: ~20–30%; Advanced
738 BioMatrix), and 0.025% (w/v) riboflavin (Sigma-Aldrich, R7774, Darmstadt, Germany)
739 (photoinitiator) on ice. The chilled MONHA hydrogel precursor solution was pipetted as 250 µl
740 into 8 x 4 mm PDMS molds or 500 µl into 10 x 6 mm PDMS molds. Constructs were then
741 crosslinked by exposure to low intensity blue light (405-500 nm) (OmniCure S1500 UV Spot
742 Curing System; Excelitas Technologies, Mississauga, Ontario, Canada) at 10.3 mW/cm^2 intensity
743 for 5 minutes. Following hydrogel crosslinking, each MONHA-encapsulated hydrogel was
744 carefully removed from its respective PDMS mold and left in MONHA growth medium [22].
745 MONHA-hydrogels were cultured for 14 days prior to any experiments, and media was
746 replenished every 2-3 days.
747
748 ***4.4 MONHA-encapsulated ECM hydrogel pore size analysis***
749 The collagen network of acellular and MONHA-encapsulated hydrogels was imaged with
750 confocal reflectance microscopy on a Zeiss LSM980 scanning confocal microscope (Carl Zeiss

751 Microscopy, Jena, Germany) using a 40x water immersion objective (LD LCI Plan-Apochromat
752 40x/1.2 Imm Corr DIC M27, Zeiss). The excitation wavelength was set to 488 nm and backscatter
753 signal was collected via a beam splitter BC80/20. Pore size within the collagen gel was calculated
754 using an algorithm as previously described [61]. In brief, 6-9 fields of view were obtained from
755 the core and periphery of MONHA-encapsulated hydrogels for each magnitude of strain (i.e., 0%,
756 3%, or 10%) at each timepoint (i.e., 4 hours, 24 hours). The image size was set to 1024 x 1024
757 pixels in x/y and the z-step interval set to 0.5 µm collecting a total of 50 µm in the z-axis direction.
758 The confocal z-stack images of the collagen gel were input to FIbeR Extraction MATLAB code
759 [62] to extract the Euclidean distance map. The pore size was then extracted using the bubble
760 analysis algorithm in MATLAB [63].
761
762 ***4.5 MONHA-encapsulated ECM hydrogel permeability analysis***
763 To determine the permeability of MONHA-encapsulated hydrogels, acellular and
764 MONHA-encapsulated hydrogels were crosslinked on top of 3 µm pore size transwell inserts in
765 12-well plates (Thermo Fisher, 141080, Kennebunk, Maine, USA). Before initiating the
766 permeabilization assay, gels were equilibrated in DMEM/F12 for 24h. The assay was initiated by
767 adding 200 µl of a 1000 µg/ml FITC-labelled dextran (70 kDa) tracer solution (FITC-DEAE-
768 Dextran; Sigma, 54702-1G) into the top chamber above each hydrogel. In the bottom chamber,
769 1000 µl Dulbecco's Phosphate Buffered Saline 1X (DPBS; Invitrogen, 14190-44) was added
770 which served as receiving medium. The tracer molecule leakage into the bottom well was
771 quantified (i.e., after permeating through the hydrogel). A volume of 600 µl from the bottom well
772 was withdrawn at each time point (5, 10, 15, 30, 45 min – 1, 2 h), and each time it was replenished
773 by an equal volume of fresh DPBS. For quantification, a standard curve was generated using

774 graded dilutions of FITC-labelled dextran (1 to 1000 μg/ml). A volume of 200 μL for each
775 supernatant sample and standard were transferred into a 96-well plate and absorbance was
776 measured at 490 nm using a BioTek Gen5 microplate reader (version 3.16; Agilent Technologies,
777 Palo Alto, CA, United States). The concentration of "leaked" FITC-labelled dextran in the
778 collected samples was determined using a standard curve equation and as previously described
779 [64, 65]. Cumulative FITC-labelled dextran at each time point was calculated by using:
780

781 Total FITC-labelled dextran in the bottom chamber before removal at time point t:$\text{Total}_t = C_t$
782 $\times 1000\mu L$; where C_t is concentration FITC-DEX at time point t.
783 Total FITC-DEX removed at time point t:$\text{Removed}_t(\mu g) = Ct \times 600\mu L$; where 600 μL= volume
784 removed.
785 Remaining FITC-DEX in the bottom well after removal at time point t:$\text{Remaining}_t\ (\mu g)=\text{Total}_t$
786 $(\mu g)-\text{Removed}_t\ (\mu g)$.
787 The cumulative leaked FITC-labelled dextran up to time point t :

788 $$\text{Cumulative}_\text{t} = \sum_{t=0}^{t} Removed_t\ (\mu g)$$

789

790 ***4.6 MONHA-encapsulated ECM hydrogel collagen fiber signal intensity, compaction and cell***
791 ***alignment analysis***

792 For collagen signal intensity and compaction analyses, MONHA-encapsulated hydrogels
793 were imaged using confocal reflectance microscopy (see **Methods 4.4**). Fold-change collagen
794 signal intensity in MONHA-encapsulated hydrogels was quantified with background subtraction
795 from an acellular hydrogel using Z-project Maximum Intensity Projection in FIJI and further
796 normalized to number of nuclei. Collagen compaction was determined as previously described

797 [66]. In brief, the mean intensity of collagen fibrils in the fixed area around the astrocytes was
798 computed and then normalized against the mean intensity of the collagen fibrils as deduced from
799 acellular collagen images. The cropped area was found with binarized fluorescent images of the
800 astrocytes with pretrained denoising convolutional neural network (dsCNN)/median filter and
801 adaptive threshold functions in MATLAB. Moreover, due to the large sample size (number of
802 pixel intensity N > 10000), we used Cohen's effect size d to compare the relative difference
803 between the mean value of different groups (i.e., substantive significance), which scales with
804 sample size unlike p-value (i.e., statistical significance) [67]. Cohen's d = 0.20, 0.50, and 0.80 was
805 used to indicate the effect size as small, medium, or large, respectively.
806
807 ***4.7 Mechanical loading of MONHA-encapsulated ECM hydrogels***
808 Using a custom bioreactor system [23-25], unconfined MONHA-encapsulated hydrogels
809 were cultured for 14 days, then subjected to either 0%, 3% or 10% cyclic compressive strain at
810 1Hz for 4 hours and 24 hours. These biomechanical strain intensities have been previously
811 correlated with strains within the glaucomatous ONH [18-20]. Hydrogels were placed on PDMS-
812 coated glass containers and maintained in 40 ml of astrocyte media for the duration of
813 biomechanical strain. A thermoplastic polyester platen attached to a linear actuator (Zaber Inc.,
814 NA08A30-T4), with 5 mm clearance from the glass wall and 10 perforations (5 mm in
815 diameter/perforation) cyclically compressed the hydrogels to 3 or 10% of their height. 0% static
816 controls were maintained in similar conditions with the platen immediately above the hydrogels,
817 but not actively compressing them. For post-strain analysis, the top 1 mm (adjacent to the
818 compressive platen) and bottom 1 mm (adjacent to the glass container) were discarded as to avoid
819 any biased effects caused by contact with the platen or glass container, and the 3 mm core was

820 further separated from the periphery of the hydrogel to allow for systematic comparisons between
821 different regions, magnitudes and durations of biomechanical strain.
822
823 ***4.8 Encapsulated MONHA cell viability analyses***
824 Cell viability within the hydrogel was determined using a CellTiter 96® Aqueous Non-
825 Radioactive Cell Proliferation Assay (MTS; Promega, Madison, WI, USA) as per the
826 manufacturer's instructions. Following 24 hours of cyclic strain, MONHA-encapsulated hydrogels
827 were incubated with the staining solution (114 µl MTS, 6 µl PMS solution, 600 µl media) at 37 °C
828 for 4h, and absorbance at 490 nm was assessed with a spectrophotometer plate reader (BioTEK,
829 Winooski, VT, USA). Fold-change over time of blank-corrected absorbance values was analyzed
830 to quantify cell viability in hydrogels.
831
832 ***4.9 Encapsulated MONHA morphological analysis***
833 Following application of compressive strain, MONHA-encapsulated hydrogels were fixed
834 with 4% PFA at 4 °C overnight, permeabilized with 0.5% Triton™ X-100 (Thermo Fisher
835 Scientific) and stained for filamentous actin (F-actin; Alexa Fluor® 488- or 594- conjugated
836 Phalloidin (1:200, Abcam, Ab176757 or Ab176753); nuclei were counterstained with DAPI.
837 Fluorescent z-stack images were captured using an air 20x objective (Plan-Apochromat 20x/0.8
838 M27, Zeiss) and a Zeiss LSM780 scanning confocal microscope (Carl Zeiss Microscopy, Jena,
839 Germany). The image size was set to 1024 x 1024 pixels or 512 x 512 in x/y, and six titled z-stack
840 images consisting of 100 µm in z-axis direction with the z-step interval set to 1.3 µm were obtained.
841 Assessment of cell morphology was conducted using Z-project Maximum Intensity Projection in
842 FIJI (NIH, Bethesda, MD) across individual z-stacks. F-actin masks were then generated and

843 binarized in FIJI, and the area of F-actin coverage was calculated by the ratio of percentage of
844 pixels with non-zero pixels [68].
845
846 ***4.10 MONHA-encapsulated ECM hydrogel sectioning and immunohistochemical analysis***
847 MONHA-encapsulated hydrogels were cultured for 14 days prior to compressive loading
848 for 4h and 24h and then fixed with 1% Pagano fixative solution (i.e., 4% PFA, 50 mM Sucrose,
849 25 mM MgCl2, 2.5 mM KCl, HEPES 7.4) [69] at 4°C overnight. Samples were then washed with
850 DPBS and embedded in 10% bovine gelatin (Sigma-Aldrich, G9382-500G). Subsequently,
851 gelatin-embedded MONHA-encapsulated hydrogels were fixed again with 1% Pagano fixative
852 solution at 4°C overnight and then washed with DBPS. Using the Leica VT1000 S vibratome, 150
853 μm sections were cut and collected in cold PBS. Sections were then permeabilized with 0.5%
854 Triton™ X-100 for 15 min, blocked in 7% normal goat serum (Abcam, Ab7481) for 1h and
855 immunostained in 1% normal goat serum (Abcam, Ab7481) for either GFAP (Anti-GFAP
856 Antibody Cy3 Conjugate, 1:100, Millipore, MAB3402C3), fibronectin (rabbit anti-fibronectin
857 antibody, 1:100, Abcam, Ab2413) or hypoxia-inducible factor 1α (HIF-1α; rabbit anti-HIF-1
858 alpha antibody, 1:200, Abcam, Ab228649) overnight, followed by stain with Alexa Fluor® 488-
859 conjugated secondary antibody (goat polyclonal antibody to rabbit IgG, 1:500, Abcam, Ab150077)
860 for 1 h; nuclei were counterstained with DAPI (Abcam, Ab228549). Sections were mounted with
861 ProLong™ Gold Antifade (Thermo Fisher Scientific, P36930, Waltham, MA, USA) on
862 Superfrost™ Plus microscope slides (Fisher Scientific, 1255015). 3-4 fields of view per core or
863 periphery of the hydrogel were acquired using an air 40x objective (S Plan Fluor 40x/0.6, Nikon)
864 and an Andor BC43 SR spinning-disk confocal microscope (Oxford Instruments, Belfast, Northern
865 Ireland). The image size was set to 2040 x 2040 pixels in x/y and the z-step interval set to 1 μm

866 collecting a total of 40 μm in the z-axis direction. Fold-changes in normalized signal intensity were
867 quantified with background subtraction using Z-project Maximum Intensity Projection in FIJI and
868 further normalized to number of nuclei for GFAP and HIF-1α analyses.
869
870 ***4.11 MONHA-encapsulated ECM hydrogel rheology analysis***
871 MONHA-encapsulated hydrogels, fabricated using the 10 x 6 mm PDMS molds, were
872 cultured for 14 days prior to application of compressive strain. Immediately following 24 hours
873 compression, viscoelasticity of MONHA-encapsulated hydrogels (N = 6 per group) was measured
874 using a Kinexus rheometer (Malvern Panalytical, Westborough, MA, USA) with an 8 mm diameter
875 parallel plate. Rheometry measurements were performed as previously described [22]. Briefly, an
876 8 mm geometry was lowered onto the hydrogels to establish a calibration normal force of 0.02 N.
877 Subsequently, an oscillatory shear-strain sweep (0.1–60%, 1.0 Hz, 25 °C) was performed to
878 determine storage modulus (G') and loss modulus (G") values within the linear viscoelastic region.
879 The storage modulus for each sample was then converted to elastic modulus (E) using the equation
880 $E = 2 * (1 + v) * G'$, assuming a Poisson's ratio (v) of 0.5 for the ECM hydrogels.
881
882 ***4.12 RNA sequencing and data sharing***
883 The 3 mm core and the remaining periphery of MONHA-encapsulated hydrogels were
884 isolated after compression for bulk RNA-sequencing. Three samples per strain group (i.e., 0%,
885 3%, 10%) at each time point (i.e., 4h, 24h) were used. Briefly, each sample was generated by
886 pooling corresponding microregions (i.e., core or periphery) from two independent MONHA-
887 encapsulated hydrogels, and then homogenized for 2 minutes using a Fisherbrand™ 150 Handheld
888 Homogenizer. Total RNA was extracted using Trizol reagent (Invitrogen, 15596026, Carlsbad,

889 CA, United States) according to the manufacturer's protocol. 250 ng of extracted RNA was used
890 as input to the Illumina Stranded mRNA Library prep kit as per the manufacturer's instructions.
891 Library quality and quantity was assessed with Agilent 2100 Bioanalyzer (Agilent Technologies,
892 Palo Alto, CA, United States). 36 libraries were pooled together for sequencing on an Illumina
893 NextSeq 2000 next-generation sequencing instrument with paired end 2x100bp. High-quality
894 clean reads were filtered into FASTQ format. RNA sequencing data is deposited and accessible
895 through NIH Gene Expression Omnibus (GEO) DataSets GSE300233.
896
897 ***4.13 Bioinformatic data analysis***
898 RNA-seq data were analysed using the online platform Illumina Partek-Flow (version
899 12.6.1) (Chesterfield, Missouri, USA). Briefly, FASTQ files were subjected to sequence quality
900 checks using "QC for Sequencing Reads" tool. Using the STAR 2.7.8a tool the reads were mapped
901 against the mouse reference genome mm39. Aligned reads were then quantified to annotation
902 model of mouse genome. Principal component analysis (PCA) of the top 2000 genes with greatest
903 variance in expression was applied to all samples to delineate clustered groups between
904 biomechanical strain durations and intensities. Differentially expressed genes (DEGs) across time
905 (i.e., 24h vs 4h) and biomechanical strain magnitude (i.e., 0% vs 3% vs 10%) as cofactors were
906 determined using ANOVA. Separately, pairwise comparisons between biomechanical strain
907 intensities (i.e., 3% vs 0%, and 10% vs 0%) at each timepoint (i.e., 4h or 24h) within each hydrogel
908 region (i.e., core or periphery) were identified using DESeq2 tool. For both analyses, the genes
909 and transcripts with FDR corrected p-value ≤ 0.05 and $|\text{Log2 fold change}| \geq 1.50$ were considered
910 differentially expressed. Gene ontology (GO) pertaining to biological process, cellular component,
911 and molecular function for each individual comparison was determined based on the over

representation analysis (ORA) using the publicly available enrichment tool WEB-based GEne SeT AnaLysis Toolkit (https://www.webgestalt.org) [70] with FDR corrected p-value ≤ 0.05. Gene Set Enrichment Analysis (GSEA) against KEGG/Reactome databases was used to delineate altered molecular pathways across time amongst all groups and significance was set to FDR corrected p-value ≤ 0.05 and |Log2 fold change| ≥ 1.50.

4.14 Statistical analyses

Statistical analyses were performed using GraphPad Prism software v10.0.2 (GraphPad Software, La Jolla, CA, USA). Experimental results are illustrated using multivariable graphs and histograms, and sample sizes are specified in each figure caption. Group comparisons were determined by one-way (ANOVA) with Tukey's multiple comparisons *post hoc* as appropriate and Cohen's effect size d as described in **Methods 2.6** [67]. All data are shown with mean ± SD. The level of significance was set to $p < 0.05$.

Disclosure

The authors report no conflicts of interest.

Funding

This project was supported in part by National Institutes of Health (NIH) grants K08EY031755 (to P.S.G.), R01EY036880 (to P.S.G.), R21EY036198 (to P.S.G.), R01EY034096 (to S.H.), R21EY036189 (to S.H.), R35GM142963 (to A.E.P.), R01EY023242 (to Y.L.), R01EY023242S (to Y.L.), R21EY033961 (to Y.L.), R01EY032960 (to Y.L.), R21EY028671 (to Y.L.), and P30EY031631 (to Y.L.), R21NS139236 (to M.V.), R01EY030567 (to A.M.B),

935 R01EY024942 (to A.M.B), and R44EY035188 (to A.M.B), as well as the Merit Review Award
936 I01BX005360 from the United States Department of Veterans Affairs (to A.M.B). It was also
937 supported by the BrightFocus Foundation G2024006S (to S.H.), the David Epstein Career
938 Advancement Award in Glaucoma Research from Research to Prevent Blindness (to S.H.),
939 unrestricted grants from Research to Prevent Blindness and Lions Region 20-Y1 to SUNY Upstate
940 Medical University Department of Ophthalmology and Visual Sciences, The Glaucoma
941 Foundation/Bright Focus Award (to A.V and A.M.B), and private foundations The Glaucoma
942 Foundation, the BrightFocus Foundation, and the Glaucoma Research Foundation (to Y.L.).
943

944 **Acknowledgments**

945 We thank the Neuroscience Microscopy Core at Upstate Medical University and the Blatt
946 BioImaging Center at Syracuse University for imaging support. We thank the laboratory of Dr.
947 Daniel J. Kelly at Trinity Centre for Biomedical Engineering, University of Dublin for their
948 guidance and support in establishing the bioreactor system in our laboratory.
949

950 **Author contributions:** A.N.S., S.P, M-T. H. T., A.K., S.G., M.P.G., A.V., A.M.B, M.V.,
951 Y.L., A.E.P., S.H. and P.S.G. designed all experiments, collected, analyzed, and interpreted the
952 data. A.N.S and P.S.G. wrote the manuscript. All authors commented on and approved the final
953 manuscript. S.H. and P.S.G conceived and supervised the research.
954

955 **Data and materials availability:** All data needed to evaluate the conclusions in the paper
956 are present in the paper and/or the Supplementary Materials, and RNAsequencing Data available

957 on NIH GEO DataSets GSE300233.. Additional data related to this paper may be requested from

958 the authors.

959

References

1. Gonzalez-Perez, O., V. Lopez-Virgen, and A. Quinones-Hinojosa, *Astrocytes: Everything but the glue.* Neuroimmunol Neuroinflamm, 2015. **2**(2): p. 115-117.
2. Escartin, C., et al., *Reactive astrocyte nomenclature, definitions, and future directions.* Nat Neurosci, 2021. **24**(3): p. 312-325.
3. Mishra, A., et al., *Astrocytes mediate neurovascular signaling to capillary pericytes but not to arterioles.* Nat Neurosci, 2016. **19**(12): p. 1619-1627.
4. Turovsky, E.A., et al., *Mechanosensory Signaling in Astrocytes.* J Neurosci, 2020. **40**(49): p. 9364-9371.
5. Choi, H.J., D. Sun, and T.C. Jakobs, *Astrocytes in the optic nerve head express putative mechanosensitive channels.* Mol Vis, 2015. **21**: p. 749-66.
6. Hu, Y., et al., *Matrix stiffness changes affect astrocyte phenotype in an in vitro injury model.* NPG Asia Materials, 2021. **13**(1): p. 35.
7. Mira, R.G., M. Lira, and W. Cerpa, *Traumatic Brain Injury: Mechanisms of Glial Response.* Front Physiol, 2021. **12**: p. 740939.
8. Weinreb, R.N., T. Aung, and F.A. Medeiros, *The pathophysiology and treatment of glaucoma: a review.* JAMA, 2014. **311**(18): p. 1901-11.
9. Nickells, R.W., et al., *Under pressure: cellular and molecular responses during glaucoma, a common neurodegeneration with axonopathy.* Annu Rev Neurosci, 2012. **35**: p. 153-79.
10. Tehrani, S., et al., *Optic Nerve Head Astrocytes Display Axon-Dependent and -Independent Reactivity in Response to Acutely Elevated Intraocular Pressure.* Invest Ophthalmol Vis Sci, 2019. **60**(1): p. 312-321.
11. Lozano, D.C., et al., *Early Optic Nerve Head Glial Proliferation and Jak-Stat Pathway Activation in Chronic Experimental Glaucoma.* Invest Ophthalmol Vis Sci, 2019. **60**(4): p. 921-932.
12. Cooper, M.L., et al., *Redistribution of metabolic resources through astrocyte networks mitigates neurodegenerative stress.* Proc Natl Acad Sci U S A, 2020. **117**(31): p. 18810-18821.
13. Tehrani, S., et al., *Astrocyte Structural and Molecular Response to Elevated Intraocular Pressure Occurs Rapidly and Precedes Axonal Tubulin Rearrangement within the Optic Nerve Head in a Rat Model.* PLoS One, 2016. **11**(11): p. e0167364.
14. Sun, D., et al., *Structural remodeling of fibrous astrocytes after axonal injury.* J Neurosci, 2010. **30**(42): p. 14008-19.
15. Hernandez, M.R., *The optic nerve head in glaucoma: role of astrocytes in tissue remodeling.* Prog Retin Eye Res, 2000. **19**(3): p. 297-321.
16. Pena, J.D., et al., *Transforming growth factor beta isoforms in human optic nerve heads.* Br J Ophthalmol, 1999. **83**(2): p. 209-18.
17. Pappenhagen, N., et al., *Stretch stress propels glutamine dependency and glycolysis in optic nerve head astrocytes.* Front Neurosci, 2022. **16**: p. 957034.
18. Korneva, A., et al., *Mechanical strain in the mouse astrocytic lamina increases after exposure to recombinant trypsin.* Acta Biomater, 2023. **163**: p. 312-325.
19. Sigal, I.A., et al., *Predicted extension, compression and shearing of optic nerve head tissues.* Exp Eye Res, 2007. **85**(3): p. 312-22.
20. Tamm, E.R., et al., *Biological aspects of axonal damage in glaucoma: A brief review.* Exp Eye Res, 2017. **157**: p. 5-12.

1006 21. Salvador-Silva, M., et al., *Responses and signaling pathways in human optic nerve head*
1007 *astrocytes exposed to hydrostatic pressure in vitro.* Glia, 2004. **45**(4): p. 364-77.
1008 22. Strat, A.N., et al., *Engineering a 3D hydrogel system to study optic nerve head astrocyte*
1009 *morphology and behavior.* Exp Eye Res, 2022. **220**: p. 109102.
1010 23. Mulvihill, J.J.E., et al., *Development of a Platform for Studying 3D Astrocyte*
1011 *Mechanobiology: Compression of Astrocytes in Collagen Gels.* Ann Biomed Eng, 2018.
1012 **46**(2): p. 365-374.
1013 24. Thorpe, S.D., et al., *Modulating gradients in regulatory signals within mesenchymal stem*
1014 *cell seeded hydrogels: a novel strategy to engineer zonal articular cartilage.* PLoS One,
1015 2013. **8**(4): p. e60764.
1016 25. McDermott, A.M., et al., *Recapitulating bone development through engineered*
1017 *mesenchymal condensations and mechanical cues for tissue regeneration.* Sci Transl Med,
1018 2019. **11**(495).
1019 26. Sun, D., et al., *The morphology and spatial arrangement of astrocytes in the optic nerve*
1020 *head of the mouse.* J Comp Neurol, 2009. **516**(1): p. 1-19.
1021 27. Lye-Barthel, M., D. Sun, and T.C. Jakobs, *Morphology of astrocytes in a glaucomatous*
1022 *optic nerve.* Invest Ophthalmol Vis Sci, 2013. **54**(2): p. 909-17.
1023 28. Tu, C., et al., *Proteomic Analysis of Charcoal-Stripped Fetal Bovine Serum Reveals*
1024 *Changes in the Insulin-like Growth Factor Signaling Pathway.* J Proteome Res, 2018.
1025 **17**(9): p. 2963-2977.
1026 29. Harris, R.C., E. Chung, and R.J. Coffey, *EGF receptor ligands.* Exp Cell Res, 2003.
1027 **284**(1): p. 2-13.
1028 30. Pitha, I., et al., *IOP and glaucoma damage: The essential role of optic nerve head and*
1029 *retinal mechanosensors.* Prog Retin Eye Res, 2024. **99**: p. 101232.
1030 31. Hernandez, M.R., H. Miao, and T. Lukas, *Astrocytes in glaucomatous optic neuropathy.*
1031 Prog Brain Res, 2008. **173**: p. 353-73.
1032 32. Kirschner, A., et al., *Mechanosensitive channel inhibition attenuates TGFbeta2-induced*
1033 *actin cytoskeletal remodeling and reactivity in mouse optic nerve head astrocytes.* Exp Eye
1034 Res, 2021. **212**: p. 108791.
1035 33. Nsiah, N.Y., et al., *Long-term HIF-1alpha stabilization reduces respiration, promotes*
1036 *mitophagy, and results in retinal cell death.* Sci Rep, 2023. **13**(1): p. 20541.
1037 34. Jassim, A.H., N.Y. Nsiah, and D.M. Inman, *Ocular Hypertension Results in Hypoxia*
1038 *within Glia and Neurons throughout the Visual Projection.* Antioxidants (Basel), 2022.
1039 **11**(5).
1040 35. Hernandez, M.R., W.M. Andrzejewska, and A.H. Neufeld, *Changes in the extracellular*
1041 *matrix of the human optic nerve head in primary open-angle glaucoma.* Am J Ophthalmol,
1042 1990. **109**(2): p. 180-8.
1043 36. Geiduschek, E.K. and C.M. McDowell, *The Fibro-Inflammatory Response in the*
1044 *Glaucomatous Optic Nerve Head.* Int J Mol Sci, 2023. **24**(17).
1045 37. Mazumder, A.G., A.M. Jule, and D. Sun, *Astrocytes of the optic nerve exhibit a region-*
1046 *specific and temporally distinct response to elevated intraocular pressure.* Mol
1047 Neurodegener, 2023. **18**(1): p. 68.
1048 38. Johnson, E.C., et al., *Global changes in optic nerve head gene expression after exposure*
1049 *to elevated intraocular pressure in a rat glaucoma model.* Invest Ophthalmol Vis Sci,
1050 2007. **48**(7): p. 3161-77.

1051 39. Sun, D., S. Moore, and T.C. Jakobs, *Optic nerve astrocyte reactivity protects function in*
1052 *experimental glaucoma and other nerve injuries.* J Exp Med, 2017. **214**(5): p. 1411-1430.
1053 40. Ricard, C.S., et al., *Selective expression of neural cell adhesion molecule (NCAM)-180 in*
1054 *optic nerve head astrocytes exposed to elevated hydrostatic pressure in vitro.* Brain Res
1055 Mol Brain Res, 2000. **81**(1-2): p. 62-79.
1056 41. Vallejo-Giraldo, C., et al., *Hydrogels for 3D Neural Tissue Models: Understanding Cell-*
1057 *Material Interactions at a Molecular Level.* Front Bioeng Biotechnol, 2020. **8**: p. 601704.
1058 42. Placone, A.L., et al., *Human astrocytes develop physiological morphology and remain*
1059 *quiescent in a novel 3D matrix.* Biomaterials, 2015. **42**: p. 134-43.
1060 43. Son, J.L., et al., *Glaucomatous optic nerve injury involves early astrocyte reactivity and*
1061 *late oligodendrocyte loss.* Glia, 2010. **58**(7): p. 780-9.
1062 44. Quillen, S., et al., *Astrocyte responses to experimental glaucoma in mouse optic nerve*
1063 *head.* PLoS One, 2020. **15**(8): p. e0238104.
1064 45. Balaratnasingam, C., et al., *Elevated pressure induced astrocyte damage in the optic nerve.*
1065 Brain Res, 2008. **1244**: p. 142-54.
1066 46. Hernandez, M.R. and H. Ye, *Glaucoma: changes in extracellular matrix in the optic nerve*
1067 *head.* Ann Med, 1993. **25**(4): p. 309-15.
1068 47. Schneider, M. and R. Fuchshofer, *The role of astrocytes in optic nerve head fibrosis in*
1069 *glaucoma.* Exp Eye Res, 2016. **142**: p. 49-55.
1070 48. Albalawi, F., et al., *The P2X7 Receptor Primes IL-1beta and the NLRP3 Inflammasome in*
1071 *Astrocytes Exposed to Mechanical Strain.* Front Cell Neurosci, 2017. **11**: p. 227.
1072 49. Lu, W., et al., *The P2X7 receptor links mechanical strain to cytokine IL-6 up-regulation*
1073 *and release in neurons and astrocytes.* J Neurochem, 2017. **141**(3): p. 436-448.
1074 50. Kirwan, R.P., et al., *Hypoxia regulated gene transcription in human optic nerve lamina*
1075 *cribrosa cells in culture.* Invest Ophthalmol Vis Sci, 2012. **53**(4): p. 2243-55.
1076 51. Mylonis, I., G. Simos, and E. Paraskeva, *Hypoxia-Inducible Factors and the Regulation of*
1077 *Lipid Metabolism.* Cells, 2019. **8**(3).
1078 52. Jassim, A.H., et al., *Oxidative Stress and Hypoxia Modify Mitochondrial Homeostasis*
1079 *During Glaucoma.* Antioxid Redox Signal, 2021. **35**(16): p. 1341-1357.
1080 53. Kamel, K., et al., *Reduced Oxidative Phosphorylation and Increased Glycolysis in Human*
1081 *Glaucoma Lamina Cribrosa Cells.* Invest Ophthalmol Vis Sci, 2020. **61**(13): p. 4.
1082 54. Beckel, J.M., et al., *Mechanosensitive release of adenosine 5'-triphosphate through*
1083 *pannexin channels and mechanosensitive upregulation of pannexin channels in optic nerve*
1084 *head astrocytes: a mechanism for purinergic involvement in chronic strain.* Glia, 2014.
1085 **62**(9): p. 1486-501.
1086 55. Mazumder, A.G., et al., *Astrocyte heterogeneity within white matter tracts and a unique*
1087 *subpopulation of optic nerve head astrocytes.* iScience, 2022. **25**(12): p. 105568.
1088 56. Howell, G.R., et al., *Axons of retinal ganglion cells are insulted in the optic nerve early in*
1089 *DBA/2J glaucoma.* J Cell Biol, 2007. **179**(7): p. 1523-37.
1090 57. Alarcon-Martinez, L., et al., *Interpericyte tunnelling nanotubes regulate neurovascular*
1091 *coupling.* Nature, 2020. **585**(7823): p. 91-95.
1092 58. Sigal, I.A., et al., *Finite element modeling of optic nerve head biomechanics.* Invest
1093 Ophthalmol Vis Sci, 2004. **45**(12): p. 4378-87.
1094 59. Sigal, I.A., et al., *Modeling individual-specific human optic nerve head biomechanics. Part*
1095 *I: IOP-induced deformations and influence of geometry.* Biomech Model Mechanobiol,
1096 2009. **8**(2): p. 85-98.

1097 60. Jin, Y., et al., *Effect of Changing Heart Rate on the Ocular Pulse and Dynamic*
1098 *Biomechanical Behavior of the Optic Nerve Head.* Invest Ophthalmol Vis Sci, 2020. **61**(4):
1099 p. 27.
1100 61. Ho Thanh, M.T., et al., *Vimentin promotes collective cell migration through collagen*
1101 *networks via increased matrix remodeling and spheroid fluidity.* bioRxiv, 2024.
1102 62. Stein, A.M., et al., *An algorithm for extracting the network geometry of three-dimensional*
1103 *collagen gels.* J Microsc, 2008. **232**(3): p. 463-75.
1104 63. Munster, S. and B. Fabry, *A simplified implementation of the bubble analysis of biopolymer*
1105 *network pores.* Biophys J, 2013. **104**(12): p. 2774-5.
1106 64. Adeoye, A.J. and E. de Alba, *A Simple Method to Determine Diffusion Coefficients in Soft*
1107 *Hydrogels for Drug Delivery and Biomedical Applications.* ACS Omega, 2025. **10**(11): p.
1108 10852-10865.
1109 65. Lepsky, V.R., et al., *FITC-Dextran Release from Cell-Embedded Fibrin Hydrogels.*
1110 Biomolecules, 2021. **11**(2).
1111 66. Coelho, N.M., et al., *MRIP Regulates the Myosin IIA Activity and DDR1 Function to*
1112 *Enable Collagen Tractional Remodeling.* Cells, 2020. **9**(7).
1113 67. Sullivan, G.M. and R. Feinn, *Using Effect Size-or Why the P Value Is Not Enough.* J Grad
1114 Med Educ, 2012. **4**(3): p. 279-82.
1115 68. Rust, R., et al., *A Practical Guide to the Automated Analysis of Vascular Growth,*
1116 *Maturation and Injury in the Brain.* Front Neurosci, 2020. **14**: p. 244.
1117 69. Nichols, A.J., et al., *Ex utero electroporation and whole hemisphere explants: a simple*
1118 *experimental method for studies of early cortical development.* J Vis Exp, 2013(74).
1119 70. Elizarraras, J.M., et al., *WebGestalt 2024: faster gene set analysis and new support for*
1120 *metabolomics and multi-omics.* Nucleic Acids Res, 2024. **52**(W1): p. W415-W421.
1121